Renewable Energy 224 (2024) 120184

Contents lists available at ScienceDirect

Renewable Energy

journal homepage: www.elsevier.com/locate/renene

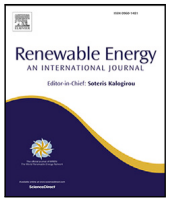

Metocean conditions at two Norwegian sites for development of offshore wind farms

Etienne Cheynet [a,*], Lin Li [b], Zhiyu Jiang [c]

[a] Geophysical Institute and Bergen Offshore Wind Centre, University of Bergen, Bergen, Norway
[b] Department of Mechanical and Structural Engineering and Materials Science, University of Stavanger, Stavanger, Norway
[c] Department of Engineering Sciences, University of Agder, NO-4879, Grimstad, Norway

ARTICLE INFO

Dataset link: https://doi.org/10.5281/zenodo.10048048, https://doi.org/10.5281/zenodo.7057407, https://doi.org/10.5281/zenodo.10048159

Keywords:
Wind energy
NORA3
Wind atlas
Metocean conditions
Offshore wind turbine

ABSTRACT

This paper examines metocean data from NORA3, a state-of-the-art wind and wave hindcast dataset for Northern Europe. Two offshore Norwegian areas, Utsira Nord (UN) and Sørlige Nordsjø II (SN2), are investigated. Both areas offer significant potential for the offshore wind sector. UN is situated in deep-sea water, suitable for floating offshore wind turbines. In contrast, SN2 lies in intermediate waters and ranks among the North Sea's most promising regions allocated for offshore wind. Data from NORA3, originally on a 3-km resolution grid, are resampled into unstructured grids spanning from 1982 to 2022. This refined dataset offers a climatology time scale with superior spatial and temporal resolution compared to most other hindcast and reanalysis databases. The study examines mean wind speed and direction across seven levels, ranging from 10 m to 750 m above the surface. Analyses of extreme wind and wave conditions have been conducted. Results reveal that UN experiences higher extreme wave heights than SN2 while the extreme wind speeds may be substantially larger at SN2 than UN. Moreover, this study establishes joint distribution models that encompass several parameters, including mean wind speed, significant wave height, wave spectral peak period, and direction difference between wind and waves. Thus, this metocean data is valuable for designing and analyzing floating wind farms over their lifecycles.

1. Introduction

Renewable energies such as wind and solar are at the heart of the solutions to meet the global challenges of energy demand and climate change. Current efforts to achieve net-zero emissions by 2050 may be insufficient to limit global warming to 1.5 °C by 2100 [1,2]. Major progress is achievable through offshore wind energy, which despite its tremendous potential [3], accounted in 2022 for 8% of the global installed wind capacity only [4]. In the net-zero emission by 2050 scenario, the wind power generation should reach 7389 TWh by 2030 whereas only 2129 TWh was produced in 2022 [5]. This milestone is currently not on track, calling for a formidable effort in the offshore wind energy sector.

In 2022, Europe's cumulative installed offshore power capacity neared 30 GW [4]. Most offshore wind farms (OWFs) were in Germany and the UK. From 2020 to 2021, the global installed offshore wind capacity grew by roughly 37%, while onshore wind grew by 9% [6]. This disparity partly indicates a higher social acceptance for offshore than onshore wind [7]. With advances in technology (e.g., larger turbines and longer blades) and industry maturity, the global levelised cost of energy (LCOE) for OWFs dropped by 59% between 2010 and 2022 [6]. However, in 2022, offshore wind remained about twice as costly as onshore wind (USD 0.081/kWh versus USD 0.033/kWh) [6].

A conventional offshore wind turbine (OWT) can be classified as either bottom-fixed or floating. Currently, most OWTs are bottom-fixed, designed for water depths of less than 60 m, while floating wind turbines (FWTs) are intended for deeper waters. However, the deployment of floating OWFs is still emerging. Hywind Scotland, commissioned in 2017, was the first commercial floating offshore wind farm with a capacity of 30 MW. In 2023, Hywind Tampen (88 MW) became Norway's first wind farm designated for powering offshore oil and gas installations.

Norway has the second largest generation potential for FWTs in the world [3] and rich industrial experience from oil and gas activities. Thanks to its deep-sea harbours, the Norwegian offshore industry has promising potential for the deployment of floating OWFs. Due to deep water and challenging seabed conditions, a bottom-fixed offshore wind farm in Norway costs more than an average European wind farm does [8].

* Corresponding author.
E-mail address: etienne.cheynet@uib.no (E. Cheynet).

https://doi.org/10.1016/j.renene.2024.120184
Received 23 October 2023; Received in revised form 24 January 2024; Accepted 19 February 2024
Available online 23 February 2024

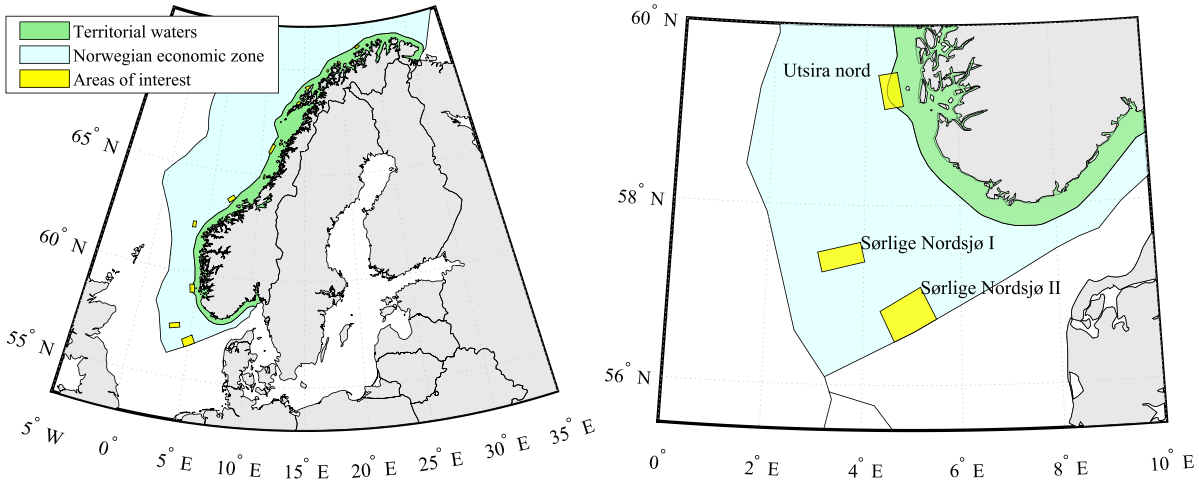

Fig. 1. Left: Areas opened for wind farm deployment in the Norwegian economic zone. Right: Close up on Sørlige Nordsjø II and Utsira Nord areas.

To facilitate the energy transition, various social, political, environmental, and technical challenges need to be tackled. From the technical side, further cost reductions and technology improvements are required of the industry through research and development, including site selection, design, construction, installation, and operation and maintenance. It is thus crucial to carry out a long-term metocean condition assessment of an offshore site before developing an OWF. In June 2020, Norway opened two offshore areas, named Utsira Nord (UN) and Sørlige Nordsjø II (SN2) for wind licensing applications. These two areas display some of the highest energy potential for the offshore wind industry in Northern Europe (see Figure 4 in Solbrekke and Sorteberg [9]). However, the detailed metocean conditions at UN and SN2 are still poorly known.

While earlier studies have highlighted the offshore wind potential in Norway [3], this paper is the first to apply the state-of-the-art hindcast NORA3, delivering a 41-year analysis of joint wind and wave conditions in UN and SN2. This analysis facilitates informed decisions potentially catalysing the growth of the offshore wind energy sector in Northern Europe. The paper primarily focuses on data analysis in key application areas such as structural design and micro-siting of OWFs, marine operations, and maintenance.

This paper is structured as follows. In Section 2, we introduce the two reference sites, namely Sørlige Nordsjø II and Utsira Nord, and the NORA3 database. Section 3 describes the significance of metocean data for the development of offshore wind farms, emphasising aspects like wind resource assessment, marine operations, design of wind turbine support structures, and layout design of wind farms. We present the methods for metocean data analysis in Section 4, highlighting spatial heterogeneity of mean wind speed, vertical wind profiles, turbulence intensity, extreme statistics of environmental parameters, and joint distributions of wind and wave characteristics. Section 5 provides an overview of the results obtained, focusing on wind and wave statistics as well as the spatial homogeneity of wind and wave characteristics. In Section 6, we explore the practical applications of the metocean data, including a case study on marine operations.

2. Reference sites and database

2.1. Sørlige Nordsjø II and Utsira Nord

In 2012, the Norwegian Water Resources and Energy Directorate assessed 15 areas for OWF development, considering impacts on ship traffic, petroleum, fisheries, and the environment [10]. By June 2020, two areas within the Norwegian economic zone, namely Utsira Nord (UN) and Sørlige Nordsjø II (SN2), opened for license applications (Fig. 1). While UN is tailored for floating wind turbine (FWT) technologies, SN2 can accommodate both floating and bottom-fixed OWTs.

SN2 lies about 140 km off the Norwegian coast, covering 2591 km^2. Conversely, UN, spanning 1010 km^2, is closer to the coast at 22 km. In February 2022, the Norwegian government proposed a total installed capacity of 3 GW for SN2 and 1.5 GW for UN. Given the proximity of SN2 to the European grid system, cross-border integration might be essential for realising SDG7 and achieving net-zero emissions by 2050 [11]. Specifically, combined grid solutions could enhance SN2's resilience and profitability [12]. Also, cooperation through bilateral trade could help mitigating potential conflicts arising from farm-to-farm wake interactions [13] especially between Norway and Denmark [14].

For SN2, the bathymetric water depth ranges between 53 m and 70 m, compatible with both FWT and bottom-fixed OWTs. UN, on the other hand, has depths from 185 m to 280 m, rendering it unsuitable for bottom-fixed OWTs. Detailed geological characteristics of UN are documented in Petrie et al. [15], while those of SN2 can be found in Petrie et al. [16]. If spar FWTs are pursued for UN, their installation might mirror the Hywind Tampen process, wherein turbines are assembled in a deep harbour and towed to their destination, a cost-effective approach [17,18]. Notably, since Hywind Tampen is 160 km from its assembly site, this method might also suit SN2, approximately 180 km from the nearest harbour (Fig. 2).

FWTs show great promise for intermediate to deep waters, but as of 2021, their presence in the North Sea remains minimal [19]. Jacket-supported OWTs are viable for SN2, though the technology has not fully matured [20]. By 2023, Dogger Bank A will house GE Haliade-X 13 MW turbines. Hence, OWTs at SN2 might surpass a 13 MW capacity with a hub height nearing 150 m above mean sea level (AMSL) [21]. Throughout this paper, "hub height" denotes 150 m above the surface unless stated otherwise.

2.2. The NORA3 database

State-of-the-art wind atlases, such as the New European Wind Atlas (NEWA) [22], ERA5 [23], and the Norwegian hindcast archive (NORA3) [24], are databases generated using numerical weather prediction models. They offer enough data to conduct a probabilistic description of wind conditions with both high temporal and spatial

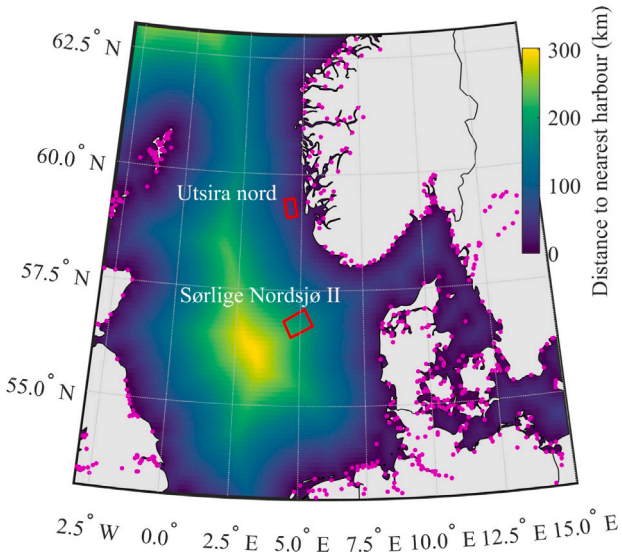

Fig. 2. Nearest distance to harbours (magenta dots) for offshore sites in the North Sea. The location of SN2 and UN are shown as red polygons. The harbour data were downloaded from the EMODnet Human Activities database.

resolutions. Thus, these databases are instrumental in the design and operation planning of future wind farms [25,26].

NORA3 is a dynamical downscaling of the ERA5 reanalysis, produced with the non-hydrostatic regional numerical weather prediction model HARMONIE-AROME. It assimilates air temperature and relative humidity data from in-situ measurements at 2 m above the surface, see Haakenstad and Breivik [27] for additional information. Since 2021, NORA3 has been publicly available.[1] The database offers wind data at a horizontal spatial resolution of 3 km and a temporal resolution of 1 h, using a hybrid sigma-pressure coordinate system. This study employs a subset of NORA3 data, with hybrid levels already converted to seven height levels at 10 m, 20 m, 50 m, 100 m, 250 m, 500 m, and 750 m above sea level. In this study, an additional eighth level at 150 m was added using piecewise cubic Hermite interpolating polynomial interpolation of the wind speed profiles.

Within the WINDSURFER project [28], NORA3 has also been applied to refine wave condition modelling in the North Sea, the Norwegian Sea, and the Barents Sea. This project modified the wave model WAM Cycle 4.7 and used NORA3 atmospheric data as forcing. Additional information on the wave model and its implementation are available in Breivik et al. [28]. This initiative resulted in an additional dataset, available since 2021,[2] detailing wave conditions with a temporal resolution of 1 h and a spatial resolution of 3 km.

The NORA3 database builds on the foundations of NORA10 [29], which has been utilised for over a decade by the offshore industry in the North Sea. As shown by Haakenstad et al. [24], NORA3 offers a significant enhancement in the description of metocean conditions compared to NORA10. The NORA3 database's validation for atmospheric data has been conducted in several studies, including the work of Solbrekke et al. [30] which used multiple oil and gas platforms and offshore masts in the North Sea and Norwegian Sea or Cheynet et al. [31] who compared NORA3 and NEWA using one year of measurements on the offshore platform FINO1. For wave data, Breivik et al. [28] also used offshore platforms and buoys in the same regions. Both studies by Solbrekke et al. [30] and Breivik et al. [28] include the Ekofisk platform located ca. 120 km on the west of SN2.

In this paper, we use NORA3 to describe the metocean conditions in the newly selected areas SN2 and UN. To the authors' knowledge, the NORA3 database has been sparsely explored for offshore wind energy applications. Metocean data from 1982 to 2022 at SN2 and UN were remotely gathered using the OPeNDAP framework, resulting in approximately 3.6×10^5 samples per grid point. The data, originally in the native computational grid, were interpolated into a new grid shaped by triangulation and unstructured mesh elements. This interpolation ensures the accurate representation of data points near boundaries and corners of each area. This new grid's domain boundaries match those of SN2 and UN, with a maximum element size of roughly 3 km. This configuration led to 753 grid points within SN2 and 317 in UN (Fig. 3).

3. Relevance of metocean data to the development of offshore wind farms

Knowledge of site-specific wind and wave conditions can influence the design and optimisation of wind turbine substructures, choice of foundation and mooring systems, as well as marine operations [see e.g. 32]. As shown in Fig. 4, the lifecycle of an OWF can be divided into five stages and site-specific metocean data are relevant to Stages 1, 3, 4, and 5. At Stage 1, metocean together with seabed conditions are used in the site assessment and wind turbine design. At Stages 3 and 5, components of OWTs including blades, tower, nacelle, and foundations are assembled and decommissioned, respectively. Various marine operation activities can also be involved, such as vessel transportation and on-site crane operations for component assembly or disassembly. As demonstrated by e.g. Verma et al. [33], Guachamin-Acero et al. [34], these operations are prone to structural failures as vessels and wind turbine components are subjected to environmental loads. Stage 4 involves routine inspections and maintenance of wind turbine components, during which maintenance vessels are affected by metocean conditions. In this section, we first select wind turbine structural design (Stage 1), marine operation (Stage 3), and wind farm layout optimisation (Stage 1) as three promising research areas. Then, we identify the most relevant metocean conditions for these developments, which are also discussed in Section 5.

3.1. Wind resource assessment

Wind resource assessment heavily depends on climatological wind speed databases to estimate the energy output and capacity factor of future wind farms [35–37]. The capacity factor of a wind turbine is defined as the ratio of actual energy produced over a given time to the nominal energy producible in that time. A high capacity factor significantly reduces the LCOE for wind farms. In 2021, the LCOE for OWFs was nearly double that of onshore farms [38], posing a challenge to the growth of the European offshore wind sector.

Mapping the LCOE of OWFs using wind atlases remains an active research area, as shown by Martinez and Iglesias [39]. Their study employed wind speed data from ERA5 (with a temporal resolution of 1 h and spatial resolution of approximately 31 km) across Europe. For offshore wind energy, sea state information is vital. Wave conditions indirectly impact the wind turbine's capacity factor by affecting downtime [40]. Hence, a meaningful reduction in OWFs' LCOE necessitates a reliable assessment of metocean conditions.

3.2. Marine operations

Marine operations are also subjected to marine environmental risks. Consider the installation of an OWF. This operation typically involves load-in, transportation, lift-off, and mating of wind turbine components. Often, it requires crane operations for offshore structural components. Such operations are constrained by weather, site conditions, and specialised equipment like blade yokes and installation vessels.

[1] https://thredds.met.no/thredds/projects/nora3.html
[2] https://thredds.met.no/thredds/projects/windsurfer.html

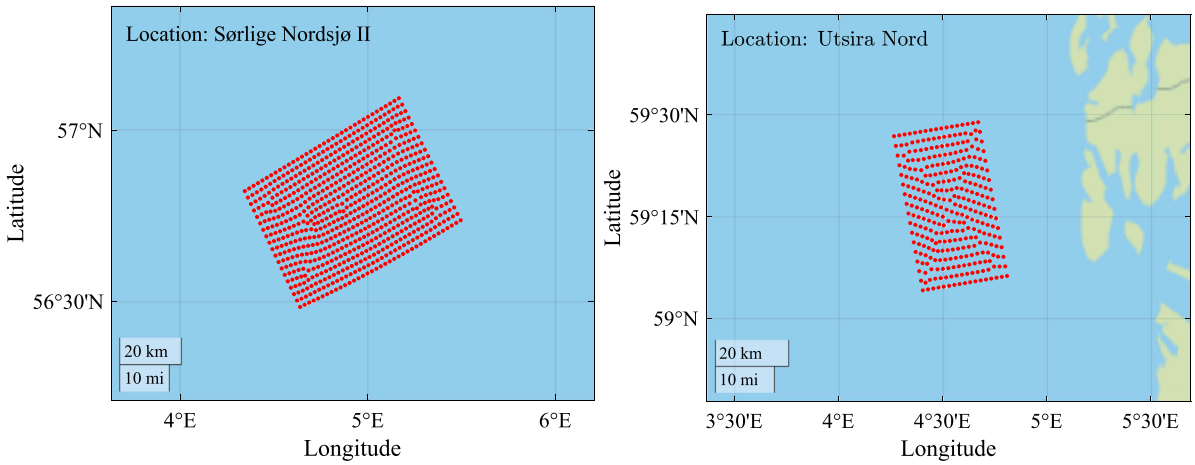

Fig. 3. Query points of the unstructured grid on which the NORA3 data have been interpolated for SN2 (top panel, 753 grid points) and UN (bottom panel, 317 grid points).

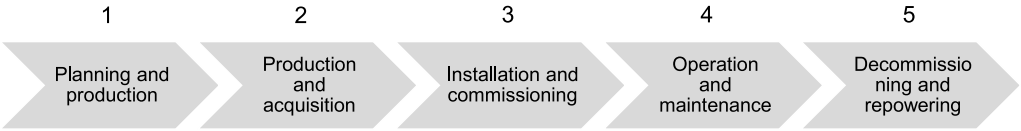

Fig. 4. Lifecycle of an offshore wind farm [17].

Knowledge of site-specific metocean conditions is crucial to determine operational limits and assess operability at the planning phase [41]. Guachamin-Acero et al. [34] highlighted how factors like wind-wave misalignment, wave height, wave period, swell, and turbulence intensity can affect operational limits, especially in blade decommissioning from an OWT. To derive operational limits based on responses, detailed simulations of the system, such as wind turbine-blade-wire-vessel, are needed.

Before undertaking such analyses, it is essential to evaluate the wind and wave conditions' spatial and annual variations at the two sites. Factors like ports, installation vessels, bathymetry, and water depths should be considered.

3.3. Design of support structures of wind turbines

The design of wind turbine structural components, such as the tower, foundations, and moorings, follows an iterative process. This procedure encompasses a global analysis of the OWT system using an aero-hydro-servo-elastic tool, semi-probabilistic failure checks in line with design standards [42], and often, a detailed structural analysis using a finite element program. Current design standards for offshore FWTs, like IEC-61400-3 [43] and DNV-ST-0119 [44], prescribe specific design load cases for these structures. These cases account for a broad spectrum of both operational and nonoperational conditions, including wind and wave loads, controller actions, and fault scenarios. The designs must satisfy checks for ultimate, fatigue, and accidental limit states.

For the ultimate limit state assessment, the most critical responses typically correspond to extreme wind and wave conditions over a specific return period, such as 50 years. These conditions can be approximated using environmental contours [45], which are rooted in offshore structure design principles. For OWTs, these contours should consider the impact of active control on load attributes [46]. Given the notable spatial and temporal wind variations at an offshore site, these variables are anticipated to affect the maximum wind loads on individual OWTs.

For the fatigue limit state, structural fatigue accumulates due to cyclic loads. The assessment necessitates the long-term distribution of external parameters, like mean wind speed and significant wave height, as inputs for frequency- or time-domain analyses [47]. The accidental limit state of OWTs is less well-defined, and standards do not clearly outline fault-related design load cases. Nonetheless, the spatial variability of the wind speed may influence the extreme wind loads experienced by the turbines [48].

3.4. Layout design of wind farms

Wind farm layout optimisation benefits significantly from the application of metocean data [49]. The optimisation problem typically involves determining the position of individual wind turbines in a farm to minimise a power-related cost function, e.g., cost of energy. Although often simplified in studies, such a cost function actually depends on influential factors including the cable layout [50,51] and installation methods [17]. Research has focused on various factors: optimisation methods [52], analytical wake models [53], and specific wind conditions [54].

For bottom-fixed OWFs, such as those supported by jackets, the turbines remain stationary. Tools like FLORIS [55] or pyWake [56] can aid the optimisation process. Conversely, floating OWFs present challenges due to the dynamic motions of the platforms under wind and wave loads. This raises concerns about the suitability of existing wake models for power estimation of floating wind farms. Therefore, the long-term distributions of wind and wave parameters, such as wind speed, wave height, and wave heading, combined with the specifications of mooring systems, are anticipated to influence the optimal layout of floating OWFs.

4. Methods for metocean data analysis

4.1. Spatial heterogeneity of mean wind speed

Offshore sites spanning a few hundred km^2 and where coastal influences on metocean conditions are negligible, typically show fairly uniform wind and wave characteristics. However, for sites like SN2 and UN, which span areas larger than 1000 km^2, this assumption may need reassessment. Accurately accounting for the spatial heterogeneity of the mean wind speed and direction is vital, not only for modelling

wind turbine and wind farm wakes [57], but also for ensuring safe maintenance operations. We propose three metrics to assess the spatial heterogeneity of the mean wind speed in SN2 and UN.

The first metric involves the earth mover's distance (EMD) [58], suitable for wind resource assessment. EMD gauges the dissimilarity between two probability distributions. For one-dimensional distributions like those considered here, the EMD represents the area between two cumulative distribution functions (CDF) F_1 and F_2:

$$\mathrm{EMD} = \int_{-\infty}^{+\infty} \left| F_1(x) - F_2(x) \right| \mathrm{d}x. \tag{1}$$

The EMD is appropriate to describe the climatology of a site and was previously employed in the NEWA design phase [22]. For our analysis, the "reference" CDF uses spatially averaged mean wind speed data from SN2 or UN.

The second metric, the spatial interquartile range (IQR), portrays the hourly spatial variability of the wind field. More suited for wind turbine operation and maintenance, this metric focuses on the heterogeneity of the mean wind conditions on shorter time scales, utilising time series and IQR statistics.

Lastly, the third metric examines the local capacity factor in comparison to the spatially averaged one. This analysis relies on the NREL 15-MW wind turbine, assuming a single turbine operation without wake effects or maintenance downtime for simplicity.

4.2. Vertical wind profiles

For wind turbine design, typical wind profiles are represented using logarithmic or power-law models [59]. These models primarily apply within the atmospheric surface layer (ASL), which constitutes about the lowest 10% of the atmospheric boundary layer (ABL). Given that the marine atmospheric boundary layer (MABL) seldom exceeds 1 km, the ASL is typically less than 100 m thick. With state-of-the-art OWTs reaching heights of up to 270 m, significant portions of their rotors frequently operate above the ASL. This suggests that the power and logarithmic laws might not be adequate for designing offshore wind turbines (OWTs) with a hub height of approximately 150 m, typical of current and future state-of-the-art large OWTs.

Over the past two decades, modified power-law or logarithmic wind speed models have emerged to broaden their applicability [60]. In this study, we employ nonlinearly interpolated wind speed profiles from the NORA3 database. We compare these profiles against the power law profile and a variant of the Deaves and Harris model [61], commonly employed for high-rise building design in the ESDU 85020 guideline [62].

In wind energy, the traditional power law is described in IEC 61400-1 [59] as:

$$\overline{u}(z) = \overline{u}_{hub} \left(\frac{z}{z_{hub}} \right)^{\alpha} \tag{2}$$

where $z_{hub} = 150$ m is the hub height selected in this study; $\overline{u}_{hub}$ is the mean wind speed at the hub height and α is the power coefficient, which depends on the atmospheric stability, surface roughness and the depth of the ABL [63].

The Deaves and Harris model is modified as:

$$\overline{u}(z) = \frac{u_*}{\kappa} \log\left(\frac{z}{z_0} \right) + p\left(\frac{z}{h} \right) \tag{3}$$

$$p\left(\frac{z}{h} \right) = a_1 \left(\frac{z}{h} \right) + a_2 \left(\frac{z}{h} \right)^2 + a_3 \left(\frac{z}{h} \right)^3 \tag{4}$$

where z is the height above sea level; $\kappa \approx 0.4$ is the von Kármán constant, h is the atmospheric boundary layer height and z_0 the roughness length; a_i, $i = \{1, 2, 3\}$ are coefficients determined empirically using the least-squares fitting method. Eq. (3) merges a classic logarithmic profile with a third-order polynomial function and is adaptable to a wide variety of wind speed profiles relevant to wind turbine and wind farm design such as non-neutral wind conditions and low-level jets prevalent in the North Sea [64].

To apply Eq. (3), the roughness length z_0 must be known. In the MABL, the surface roughness z_0 depends on the sea state and will increase as wave heights grow due to increasing surface stress. In Eq. (3), the friction velocity is estimated using Charnock's relationship [65],

$$z_0 = \frac{a}{g} u_*^2 \tag{5}$$

where $g = 9.81\ \mathrm{ms}^{-2}$ is the acceleration of gravity and a is an empirical coefficient with values between 0.01 and 0.02 [66, p. 145]. In the present case, $a = 0.014$ was chosen. Combining the neutral logarithmic wind speed profile and Eq. (5) leads to:

$$z_0 - \frac{a}{g} \left[\frac{\kappa \overline{u}(z_r)}{\ln\left(z_r / z_0 \right)} \right]^2 = 0 \tag{6}$$

which is solved numerically for $z_r = 10$ m.

Both Eqs. (2) and (3) are fitted to wind speed data from NORA3 at five different altitudes, ranging from 10 m to 500 m. In this context, the variable h is absorbed by the coefficient a_i when fitting Eq. (3), rendering explicit estimation of h unnecessary. However, this implies that a_i is influenced by both atmospheric stability and h.

4.3. Turbulence intensity

Understanding atmospheric turbulence is crucial to both structural design and power production of OWTs [67]. While the primary focus of NORA3 is on studying mean wind conditions, it also offers insights into the friction velocity and surface drag coefficient. However, to the authors' knowledge, these variables have not been cross-validated with in-situ measurements. Conducting such a validation, akin to what Renfrew et al. [68] did for the ERA5 database, would be highly valuable for both the scientific and engineering communities.

The friction velocity is often used as a scaling velocity in the Atmospheric Surface Layer (ASL) [69]. In wind energy, the standard deviation of the along-wind component, symbolised by σ_u, is more widely adopted. Specifically, design standards, e.g., [43,59], define σ_u at hub height via the turbulence intensity I_u as:

$$I_u = \frac{\sigma_u}{\overline{u}} \tag{7}$$

where $\overline{u}$ is the mean wind speed at hub height. In IEC [43], σ_u requires knowledge of the sea surface roughness z_0, which can be estimated using Eq. (6). The value for σ_u proposed by IEC [43] is generally on the conservative side as it accounts for the 90th percentile of the variance distribution [e.g.70] and is computed for hourly statistics as:

$$\sigma_u = \frac{\overline{u}_{hub}}{\log\left(z_{hub} / z_0 \right)} + 1.28 \times 1.44 \times I_{15} + 0.2 \tag{8}$$

where I_{15} is the turbulence intensity at hub height with $\overline{u}_{hub} = 15$ m s^{-1}.

Alternative turbulence intensity models can be found in sources such as the NORSOK standards [71] based on the linear model by Andersen and Løvseth [72]. The latter model was developed for moderate and strong wind conditions on Frøya island in mid-Norway with a 40-minute averaging time and a maximum height of 40 m. It is given by:

$$I_u = 0.087 \left[1 + 0.302 \left(\frac{\overline{u}(z)}{10} - 1 \right) \right] \left(\frac{z}{10} \right)^{-0.2} \tag{9}$$

where $\overline{u}(z)$ is a local measure of the mean wind speed at height z.

4.4. Extreme statistics of environmental parameters

For an accurate quantification of extreme wind speed and wave height using probabilistic methods, it is essential to define the marginal distributions of the relevant environmental parameters. Hereinafter, the

mean wind speed at hub height, $\bar{u}_{hub}$ and significant wave height (H_s) for the total sea are considered. The extreme value analysis can be performed based on several approaches. The commonly used methods include the initial distribution (ID) method, the peak over threshold (POT) method, and the block maxima (BM) method [73].

The ID method is also known as the all-sea-state method for wave height analysis. This method utilises all available data from the observations over a long period, and a temporal resolution of 3 h is usually considered for each data point. The POT method focuses on observations over a defined threshold. The BM approach is based on annual extremes or seasonal extremes. There is a trade-off when selecting the method. While the ID method utilises more data, there is a correlation between the observations, especially when the temporal resolution is high. Moreover, it is challenging to adequately discriminate the tail behaviour when fitting all data to probability distributions. In contrast, extreme events are more independent, but a lack of extreme data (e.g., annual maxima) increases statistical uncertainty. The POT method is considered a preferred model for cases in which the weather is relatively calm most of the time with few intense events. Based on the recommended practice [73], different methods should be employed and compared to provide a reasonable estimate of extremes. In this study, these three methods are applied to predict the extreme $\bar{u}_{hub}$ and H_s for the two reference sites.

The statistics based on POT methods are sensitive to the adopted threshold level. The threshold must be high enough such that the peaks over the threshold can converge for a certain probability model. Meanwhile, the sample size should be large enough to ensure a sufficient number of data points for the fitting. For an environmental parameter (X), only storms with values higher than a threshold value x_0 are considered using this method. A new variable, Y_p, needs to be established and fitted to a probability distribution model.

$$Y_p = X_p - x_0 \tag{10}$$

where X_p denotes the storm peaks for the target environmental parameter over the selected threshold value x_0.

Due to the inherent uncertainties of environmental parameters, different distribution types and fitting methods need to be evaluated for the hindcast data, and it is always challenging to evaluate the goodness of fitting. Even using the same method for the same environmental parameter, the suitable distribution types for different sites may still be different. In this study, the most suitable distribution types which give the lowest chi-square error are selected. The hybrid Lonowe model [74] is applied to fit H_s data when using the ID approach. This model assumes that the lower part of the data follows a Lognormal distribution while the upper part follows a Weibull distribution. The hybrid Lonowe model provides a better fit compared to the Weibull models, especially in the upper tail region. The probability density function (PDF) of the Lonowe model is given in Eq. (14). Both the Gumbel and Weibull distributions are compared for POT and BM based on the annual extremes. The PDF of the Weibull distribution is given in Eq. (25), and the CDF of Gumbel distribution is given as:

$$F_X(x) = \exp\left[-\exp-\left(\frac{x-\mu_X}{\beta_X}\right)\right] \tag{11}$$

where μ_X and β_X are location and scale parameters, respectively. When the long-term distribution of the environmental parameter X is established, the extreme value x_{ext} can be calculated by solving:

$$1 - F_X(x_{ext}) = \frac{1}{N_m} \tag{12}$$

where $F_X()$ is the long-term CDF of the environmental parameter using either of the methods discussed above. N_m is the total number of events within a return period of m years and is dependent on the method applied. While N_m equals to the number of all events within m years for the ID method, it equals the number of storm peaks or extreme events for the POT or the BM methods.

4.5. Joint distributions of wind and wave parameters

When performing ultimate load and fatigue damage assessments for OWTs, joint distributions of various metocean parameters are required as inputs to numerical simulations. In this study, the conditional modelling approach is applied [75,76]. It should be noted that when modelling joint distributions, we do not use hourly sampled data, but use wind and wave data with a 3-hour temporal resolution. This adjustment is made to reduce data correlation while ensuring a sufficiently large dataset for fitting the conditional distributions. The following three joint distributions for the two reference sites are established.

- Joint distribution of H_s, $\bar{u}_{hub}$ and T_p.
- Joint distribution of H_s and T_p.
- Joint distribution of $\bar{u}_{hub}$ and direction difference between wind and waves.

When establishing the Joint distribution of H_s, $\bar{u}_{hub}$ and spectral peak period (T_p), H_s is considered as the main parameter here. Thus, the joint distribution consists of a marginal distribution of H_s, a conditional distribution of $\bar{u}_{hub}$ given H_s and a conditional distribution of T_p given H_s.

$$f_{H_s,\bar{u}_{hub},T_p}(h,u,t) = f_{H_s}(h)\cdot f_{\bar{u}_{hub}|H_s}(u|h)\cdot f_{T_p|H_s}(t|h) \tag{13}$$

The procedure for establishing the joint distribution follows Li et al. [77] and Johannessen et al. [78]. The hybrid Lonowe model [74] is applied to the marginal distribution of $f_{H_s}(h)$. The PDF is given as

$$f_{H_s}(h) = \begin{cases} \dfrac{1}{\sqrt{2\pi}\sigma_{HM}h}\exp\left[-\dfrac{1}{2}\left(\dfrac{ln(h)-\mu_{HM}}{\sigma_{HM}}\right)^2\right], & h \le h_0 \\ \dfrac{\alpha_{HM}}{\beta_{HM}}\left(\dfrac{h}{\beta_{HM}}\right)^{\alpha_{HM}-1}\exp\left[-\left(\dfrac{h}{\beta_{HM}}\right)^{\alpha_{HM}}\right], & h > h_0 \end{cases}. \tag{14}$$

where μ_{HM} and σ_{HM} are the parameters for the Lognormal distribution, which are the expected value and standard deviation of the variable's natural logarithm, $ln(h)$. α_{HM} and β_{HM} are the shape and scale parameters for the two-parameter Weibull distribution. h_0 is the shifting point between Lognormal and Weibull distribution.

The conditional PDF of $\bar{u}_{hub}$ given H_s follows the two-parameter Weibull distribution:

$$f_{\bar{u}_{hub}|H_s}(u|h) = \frac{\alpha_{UC}}{\beta_{UC}}\left(\frac{u}{\beta_{UC}}\right)^{\alpha_{UC}-1}\exp\left[-\left(\frac{u}{\beta_{UC}}\right)^{\alpha_{UC}}\right] \tag{15}$$

To describe the conditionality of $\bar{u}_{hub}$ on H_s, the shape parameter α_{UC} and the scale parameter β_{UC} are fitted to smooth functions of H_s as

$$\alpha_{UC} = a_1 + \frac{a_2}{a_3 + \exp(-h)} \tag{16}$$

$$\alpha_{UC} = a_1 + a_2\cdot h^{a_3} \tag{17}$$

$$\beta_{UC} = b_1 + b_2\cdot h^{b_3} \tag{18}$$

where a_i and b_i ($i = 1,2,3$) are the fitted coefficients based on a nonlinear fitting of the parameters to the above functions. Eq. (16) is applied to fit the shape parameter for SN2, while Eq. (17) is applied for UN.

For the conditional distribution of T_p given H_s, the data follow a Lognormal distribution:

$$f_{T_p|H_s}(t|h) = \frac{1}{\sqrt{2\pi}\sigma_{TC}t}\exp\left[-\frac{1}{2}\left(\frac{ln(t)-\mu_{TC}}{\sigma_{TC}}\right)^2\right] \tag{19}$$

Similar to the conditional distribution of $\bar{u}_{hub}$ given H_s, to describe the conditionality of T_p on H_s, the mean value and the variance of $ln(t)$, i.e., μ_{TC} and σ^2_{TC} in Eq. (19) are fitted to smooth functions of H_s:

$$\mu_{TC} = c_1 + c_2\cdot h^{c_3} \tag{20}$$

$$\sigma_{TC}^2 = d_1 + d_2 \cdot \exp\left(d_3 h\right) \tag{21}$$

where c_i and d_i $(i = 1, 2, 3)$ are the fitted coefficients based on a nonlinear fitting of the parameters to the above functions.

For marine operations dominated by waves, the joint distribution of H_s and T_p for the total sea (swell plus wind sea) can also be obtained from the previously established joint distribution with three variables. The joint PDF of H_s and T_p is given as

$$f_{H_s,T_p}(h,t) = f_{H_s}(h) \cdot f_{T_p|H_s}(t|h) \tag{22}$$

As discussed earlier, the hybrid Lonowe model is applied to the marginal distribution of $f_{H_s}(h)$; see Eq. (14). For the conditional distribution of T_p given H_s, Lognormal distribution is used and details are found in Eq. (19) to Eq. (21).

Additionally, the direction differences, i.e., the misalignment angle, Δ_θ, between wind and waves may cause increased dynamic responses of the tower in the side–side direction due to less damping compared to the fore-aft direction. Studies have reported that neglecting the wind-wave misalignment will underestimate the tower base bending moment, the fatigue damage, and other structural responses [79,80]. Joint distributions of the mean wind speed at the 150-m level, $\bar{u}_{hub}$, and the misalignment angle have been established. Δ_θ is defined as the difference between the mean wind direction at 150 m height, Dir_U, and the wave direction for the total sea, Dir_W.

$$\Delta_\theta = Dir_U - Dir_W, \Delta_\theta \in [-\pi, \pi], (\text{rad}) \tag{23}$$

The joint PDF of $\bar{u}_{hub}$ and Δ_θ consists of the marginal distribution of $\bar{u}_{hub}$, $f_{\bar{u}_{hub}}(u)$ and the conditional distribution of Δ_θ given $\bar{u}_{hub}$, $f_{\Delta_\theta|\bar{u}_{hub}}(\theta|u)$.

$$f_{\bar{u}_{hub},\Delta_\theta}(u,\theta) = f_{\bar{u}_{hub}}(u) \cdot f_{\Delta_\theta|\bar{u}_{hub}}(\theta|u) \tag{24}$$

$f_{\bar{u}_{hub}}(u)$ follows the Weibull distribution with shape parameter α_{UM}, scale parameter β_{UM} and location parameter γ_{UM}.

$$f_{\bar{u}_{hub}}(u) = \frac{\alpha_{UM}}{\beta_{UM}} \left(\frac{u-\gamma_{UM}}{\beta_{UM}}\right)^{\alpha_{UM}-1} \exp\left[-\left(\frac{u-\gamma_{UM}}{\beta_{UM}}\right)^{\alpha_{UM}}\right] \tag{25}$$

Regarding the conditional distribution of the misalignment angle Δ_θ given $\bar{u}_{hub}$, various distribution models have been proposed and discussed, including the Beta distribution [81], the Von Mises distribution [79,82], and the Lognormal distribution [83]. In this study, these distribution models have been tested, but the quality of fitting is marginal. Instead, the Normal distribution is found to have better fittings on the conditional data for the reference sites compared to the previously proposed distribution models. Moreover, it was observed during the fitting process that this conditional distribution PDF does not always appear evenly distributed around the mean. For the UN site, at high wind classes (above around 26 m s^{-1}) the conditional distribution of Δ_θ is positively skewed with long tails to the right side of the distribution, indicating that an asymmetric distribution should be used. However, as the Normal distribution fits well Δ_θ for most of the wind classes and a continuous PDF is preferred for design purposes, the Normal distribution is applied to all wind classes for the conditional distribution of Δ_θ.

$$f_{\Delta_\theta|\bar{u}_{hub}}(\theta|u) = \frac{1}{\sigma_{\Theta C}\sqrt{2\pi}} \exp\left[-\frac{1}{2}\left(\frac{\theta-\mu_{\Theta C}}{\sigma_{\Theta C}}\right)^2\right] \tag{26}$$

To describe the conditionality of Δ_θ on $\bar{u}_{hub}$, the mean $\mu_{\Theta C}$ and the standard deviation $\sigma_{\Theta C}$ in Eq. (26) are fitted to smooth functions of $\bar{u}_{hub}$.

$$\mu_{\Theta C} = e_1 + e_2 \cdot \exp\left(e_3 u\right) \tag{27}$$

$$\sigma_{\Theta C} = f_1 + f_2 \cdot \exp\left(f_3 u\right) \tag{28}$$

where e_i and f_i $(i = 1, 2, 3)$ are the fitted coefficients based on a nonlinear fitting of the parameters to the above functions.

5. Results

Understanding wave conditions is critical for offshore wind energy [84]. Sea states impact stakeholders such as port facilities, wind farm operators, and vessel suppliers [85]. Thus, this study examines both wind and wave conditions.

5.1. Wind and wave statistics

Climatological mean wind direction and speed for UN and SN2 are presented in Fig. 5. Wind speeds displayed range from the typical cut-in speed of 4 m s^{-1} to the cut-off speed of 25 m s^{-1}. At UN, coastal influence is evident as the wind flow aligns generally with the coastline. In contrast, the coastline barely affects the wind direction at SN2. The bottom panels of Fig. 5 present the yearly and average Weibull distributions of mean wind speeds. Using a kernel density estimator, the PDF of the mean wind speed follows a two-parameter Weibull distribution with scale parameter a and shape parameter b. Annual data from 1982–2022 are consistent, with few deviations from the climatological average. The median wind speed at 150 m asl at SN2 is 10.3 m s^{-1}, showcasing its high offshore wind energy potential. In comparison, UN's median speed at 150 m is 9.7 m s^{-1}.

Fig. 5 displays also the wave roses for H_s and T_p across the entire sea. At UN, the coastline more significantly influences the wave direction compared to SN2. Notably, the angle between the wind direction and the wave heading remains below 50° for 70% of the time at UN and 78% at SN2.

5.2. Wind and wave spatial homogeneity

Fig. 6 illustrates the EMD values for UN and SN2. High EMD values indicate pronounced spatial heterogeneity. For SN2, the 99th percentile EMD is only 0.1 m s^{-1}, suggesting homogeneous climatological wind conditions. This low EMD is attributed to SN2's spatial dimension aligning with mesoscale atmospheric motion. UN has a slightly higher EMD, likely due to its proximity to the coast.

On 5 December 2011, the spatial variability at SN2 was notably high, with an IQR value exceeding 6 m s^{-1} (Fig. 7). However, from 1982 to 2022, less than 0.5% of samples at Utsira Nord and SN2 surpassed an IQR of 5 m s^{-1}. As Fig. 8 shows, for heights of 10 m, 100 m, and 250 m, the IQR remains below 1.5 m s^{-1} 90% of the time, suggesting largely consistent wind conditions.

SN2 has idealised capacity factor p1 and p99 values of 64% and 65%, respectively, denoting uniform power production. At UN, the respective values are 57% and 60%, indicating the necessity to consider spatial variability when assessing the LCOE of UN.

Table 1 shows the heterogeneity of H_s and T_p at both sites, quantified using the same metrics discussed in Section 5.1 - EMD and IQR. The 90th percentile of the IQR, denoted as p_{90}IQR, indicates substantial variability in the peak period across the area at times. This variation should be considered when planning safe docking operations between vessels and OWTs, as they depend critically on T_p [86]. Apart from this, both H_s and T_p exhibit relative homogeneity at SN2 and UN.

5.3. Wind speed profiles

Fig. 9 compares wind speeds from NORA3 at UN with Eqs. (3) and (2) at altitudes of 50 m, 100 m, and 250 m. Results at SN2 are similar but omitted for brevity. Eq. (3), with its larger parameter set, offers a better fit than Eq. (2). The power law model deviates significantly when the mean wind speed at hub height is below 12 m s^{-1}, making it less reliable for fatigue life assessments of OWTs.

For fatigue design, wind speed profiles can be modelled using the modified Deaves and Harris model as in Eq. (3). In this context, we advocate a data-driven modelling approach over a probabilistic one.

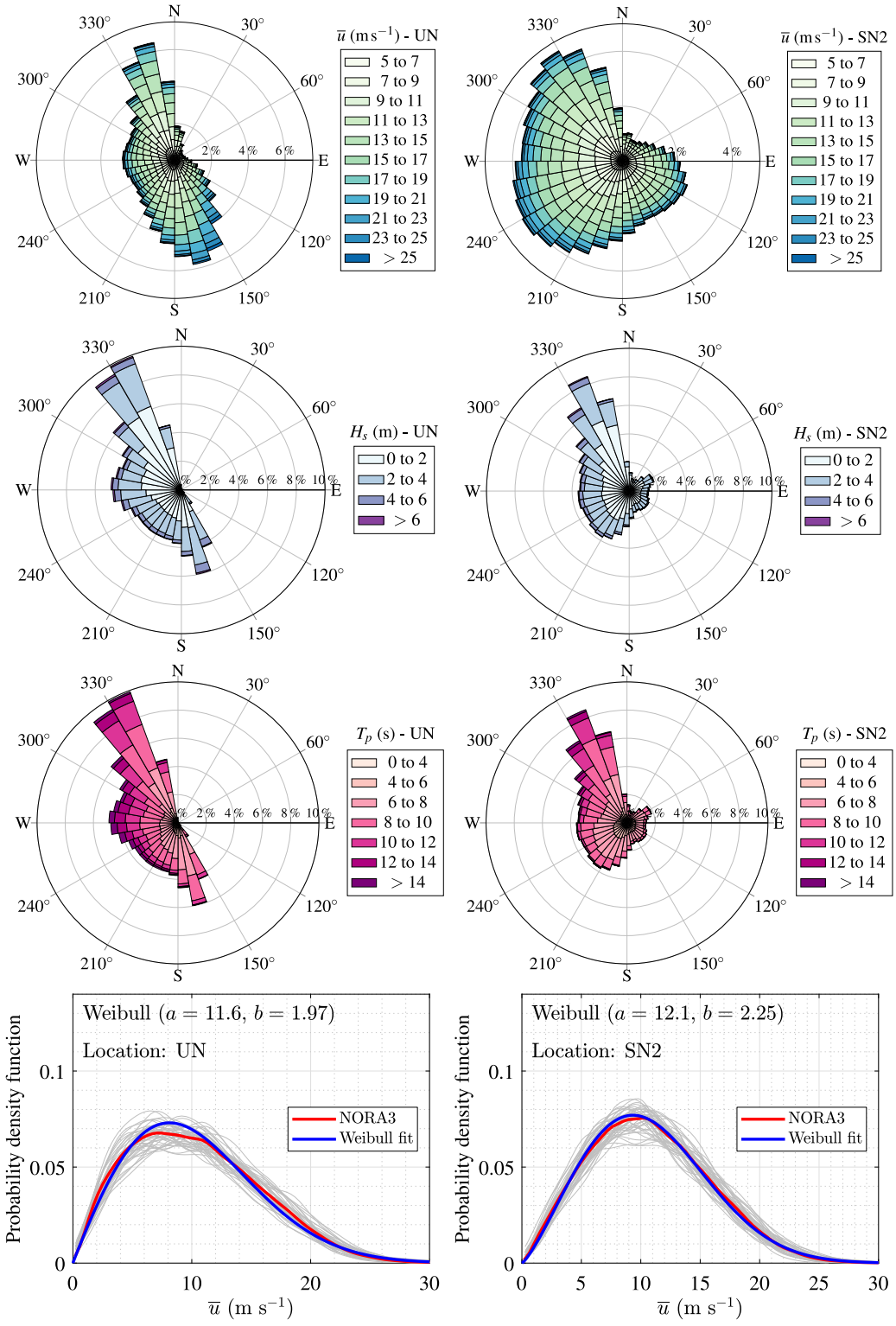

Fig. 5. Top three panels: Polar histograms of the mean wind speed at 150 m asl, H_s and T_p at UN (left panels) and SN2 (right panels) using hourly data from NORA3 from 1982 to 2022. The mean wind speed is shown as a function of the mean wind direction whereas the wave conditions are shown as a function of the wave heading. Bottom panels: Probability density function (PDF) of the mean wind speed (red solid line) fitted by a Weibull distribution (blue solid line). The grey lines correspond to the PDFs of yearly data from 1982 to 2022.

Implementing reduced-order modelling for optimising turbine dynamics is crucial, and its effectiveness heavily relies on the data-driven strategy emphasised in this study. A comprehensive database of smooth mean wind speed profiles based on Eq. (3), is openly available for both UN and SN2 on Zenodo. More generally, this dataset presents the detailed metocean conditions for the two areas of interest and complements a previous data set provided by Solbrekke and Sorteberg [9].

The power law model is rather effective for $\overline{u}_{hub} > 15$ m s^{-1}, making it potentialy suitable for extreme load analysis. For wind speeds exceeding 15 m s^{-1} at 150 m, Fig. 10 illustrates that the power law coefficient distribution can be captured using a mixture of two Gaussian

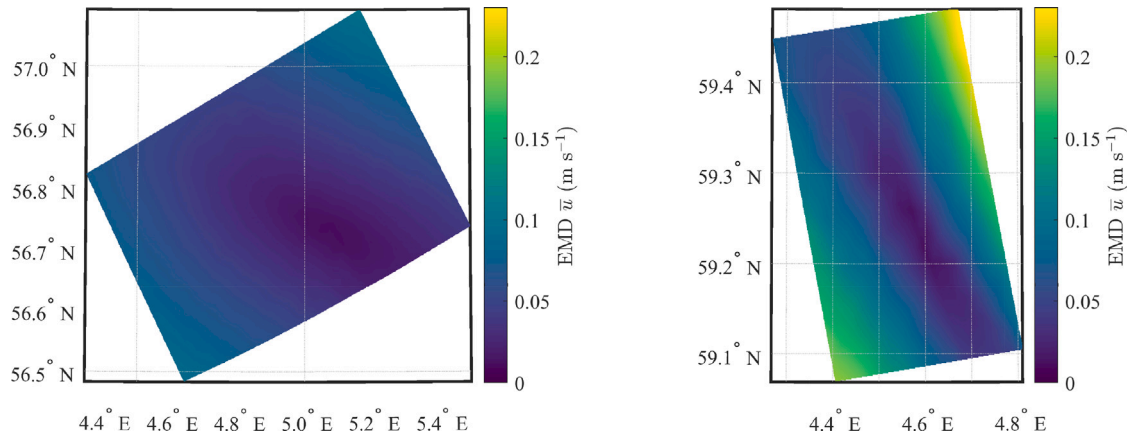

Fig. 6. Earth mover's distance (EMD) between the spatially averaged mean wind speed and the local one at SN2 (top) and UN (bottom). Data were collected using NORA3 from 1982 to 2022 and interpolated at 150 m.

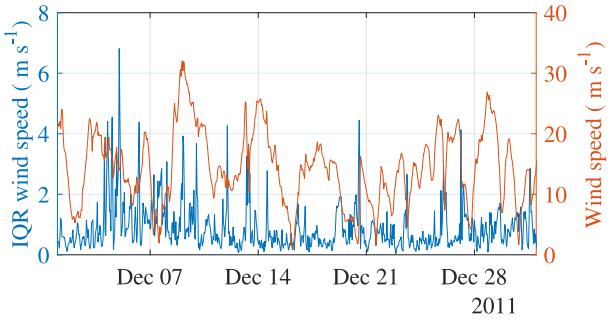

Fig. 7. Hourly variations of the spatial interquartile range of the mean wind speed, computed using 753 grid points in SN2, at 150 m above sea level.

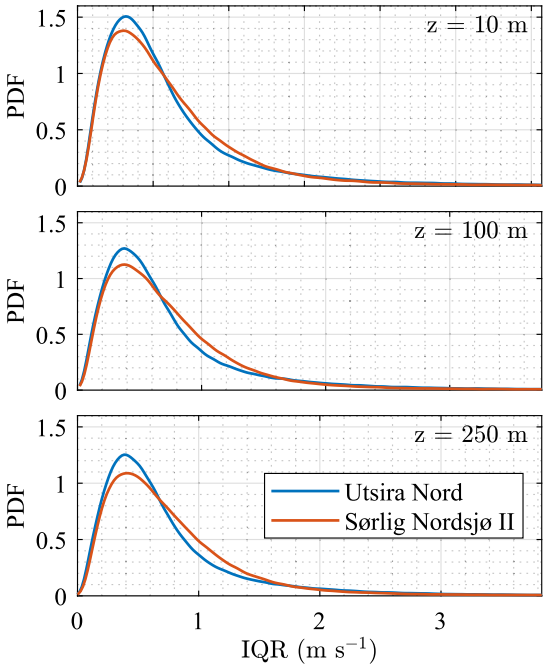

Fig. 8. Probability density function (PDF) of the interquartile range (IQR) of the mean wind speed for Sørlige Nordsjø II (SN2) and Utsira Nord (UN) at 10 m (top panel), 100 m (middle panel) and 250 m (bottom panel). The IQR is computed using the spatial average. The PDF is calculated using the time series of the IQR. Data were collected using NORA3 from 1982 to 2022 (3.6×10^5 samples).

Table 1
Values of Earth Mover's Distance (EMD) and the 90th percentile of the interquartile range (p_{90}IQR) for significant wave height (H_s) and peak period (T_p) at UN and SN2. The EMD represents the heterogeneity of H_s and T_p in terms of probability distributions, while the p_{90}IQR indicates any significant spatial variations within an hour.

Areas	UN	SN2
EMD H_s (m)	0.09	0.05
p_{90}IQR H_s (m)	0.20	0.20
EMD T_p (s)	0.20	0.29
p_{90}IQR T_p (s)	0.60	0.30

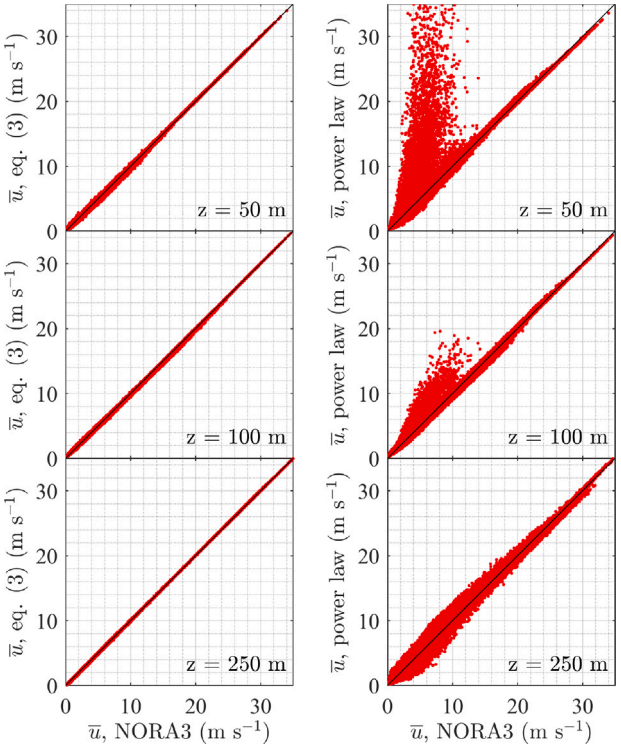

Fig. 9. Comparison of the mean wind speed from NORA3 with the modified Deaves & Harris model (left panels, Eq. (3)) and the power law (right panels, Eq. (2)) at Utsira Nord. Data were collected using 3.6×10^5 samples from 1982 to 2022.

Table 2
Parameters of the Gaussian mixture (Eq. (29)) to describe the distribution of power coefficient at UN and SN2 for a mean wind speed above 15 m s^{-1} at hub height.

Areas	p	μ_1	μ_2	σ_1	σ_2
UN	0.661	0.070	0.129	0.014	0.039
SN2	0.584	0.071	0.141	0.014	0.034

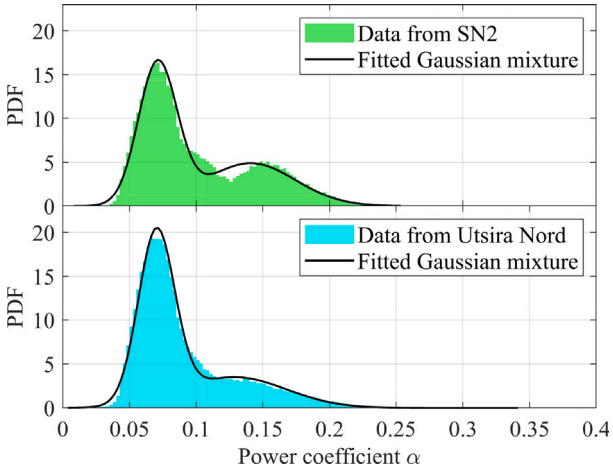

Fig. 10. Probability density function (PDF) of the power coefficients at Utsira Nord and SN2 using wind speed data above 15 m s^{-1} at 150 m only (7.3×10^4 samples from 1982 to 2022) and a bin width of 0.0025.

distributions:

$$f(x) = p\phi(x, \mu_1, \sigma_1^2) + (1-p)\,\phi(x, \mu_2, \sigma_2^2) \tag{29}$$

where p is the mixture ratio with values between 0 and 1; $\phi(x, \mu_i, \sigma_i^2)$, $i = \{1, 2\}$ is the Gaussian probability density function of variable x with a mean μ_i and variance σ_i^2.

The parameters p, σ_i, and μ_i were estimated using the maximum likelihood estimation method [87]. Their values are detailed in Table 2 for both SN2 and UN. The good agreement between modelled and estimated distribution of the power coefficient facilitates the probabilistic modelling of extreme wind loads on OWTs. The median value for the power coefficient α stands at 0.08 at both sites. This mirrors the value referred to by Furevik and Haakenstad [88], which is grounded on NORSOK [71] for offshore locations. Within the MABL, $\alpha \approx 0.11$ is a commonly-used power coefficient value [89]. Further insights about this coefficient are available in Gualtieri [90]. Our findings show that extrapolating wind speeds from 10 m to 150 m asl using the power law in the absence of tall profiles data introduces significant uncertainties, a result echoed in previous research [e.g.91].

5.4. Turbulence intensity

Fig. 11 depicts the standard deviation, σ_u, of the along-wind component as a function of the wind speed. This representation encompasses predictions from Eqs. (8) and (9), as well as in-situ estimates of σ_u derived from hourly high-frequency velocity data collected at the offshore platform FINO1 between 2007 and 2008 [92]. The figure suggests that the turbulence intensity model from IEC [43] might be overly conservative.

In the depiction of the FINO1 data in Fig. 11, σ_u was computed for $z_{hub} = 80$ m and $I_{15} = 0.07$. Notably, Eq. (9) agrees well with the variation of σ_u against the mean wind speed at FINO1, suggesting that the turbulence characteristics far offshore may not always be site-specific when viewed statistically. The term "far offshore" implies here that the influence of the coastline on the flow characteristics is negligible.

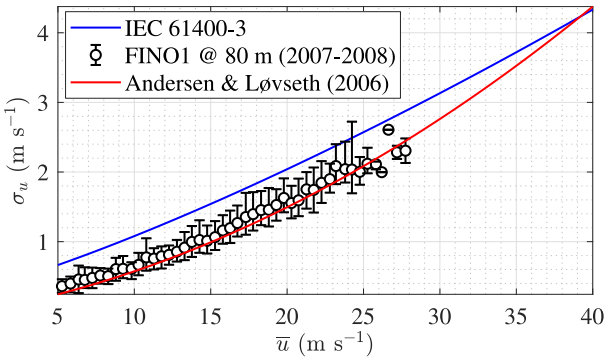

Fig. 11. Variation of the hourly standard deviation of the along-wind component with the mean wind speed. The data from the FINO1 platform are for stationary, neutral atmosphere collected in 2007 and 2008 at 80 m AMSL (2×10^3 hours of data). The errorbar represents the 10th and 90th percentiles.

Applying Eq. (9) might enhance the initial design of OWTs at SN2 and UN. This equation draws upon the local mean wind speed, obtainable from the NORA3 dataset. It remains to be ascertained whether Eq. (9) is effective at $z_{hub} = 150$ m.

Accurate estimates of $\overline{u}$ and σ_u at an OWT's hub height are crucial for scaling both the velocity spectrum and turbulence coherence, which are governing the wind loading on structures. The coherence of turbulence quantifies the spatial correlation of velocity fluctuations. The one-point velocity spectrum describes how much wind velocity fluctuates at different frequencies. The IEC 61400-1 standard [59], used for wind turbine design, mentions the possibility to use the Mann uniform shear (US) model [93] for turbulence modelling. This model quantifies the second-order structure of turbulence using only three tunable parameters. In this model, the coherence of turbulence is mainly governed by the Mann length scale parameter L. As noted by Kelly [94], tuning the US model could be effectively achieved by using the mean wind shear $\mathrm{d}\overline{u}/\mathrm{d}z$ and σ_u. In the absence of in situ measurements, $\mathrm{d}\overline{u}/\mathrm{d}z$ and σ_u might be inferred from the NORA3 database and Eq. (9), respectively. Therefore, by combining Kelly's method [94], Eq. (9), and the NORA3 database, both the length scale parameter L and the coherence of turbulence may be assessed in the preliminary design of offshore wind turbines.

Turbulence modelling in the MABL for wind energy is not without its challenges. Many standards and codes neglect non-neutral and non-stationary conditions, despite their potential impact on the fatigue life of OWTs [19,95–99]. Also, the current understanding of turbulence's spectral structure in the MABL remains limited, especially above 100 m [100].

5.5. Extreme statistics of environmental parameters

The extreme values of $\overline{u}_{hub}$ and H_s for the two sites are estimated using three methods, i.e, the ID method, the POT method and the BM method. Given that 41 years of data is available, annual maxima are applied for the BM method. When applying POT, sensitive studies on threshold levels have been performed to fit storm peaks for $\overline{u}_{hub}$ and H_s, respectively. In general, the fitted parameters as well as the extreme values are sensitive to threshold values, as discussed in Mackay et al. [101] or Vanem [102]. In this study, the thresholds for the two environmental parameters are selected to ensure a sufficient number of storm peaks and meantime the fitted distribution parameters are relatively stable with respect to the changing threshold level near the selected values.

Table 3 compares the estimated spatially averaged 50- and 100-year extreme values for $\overline{u}_{hub}$ and H_s using different methods. As seen, the extreme values are sensitive to the choice of method. The selection of distribution types and the uncertainties during the fitting procedure

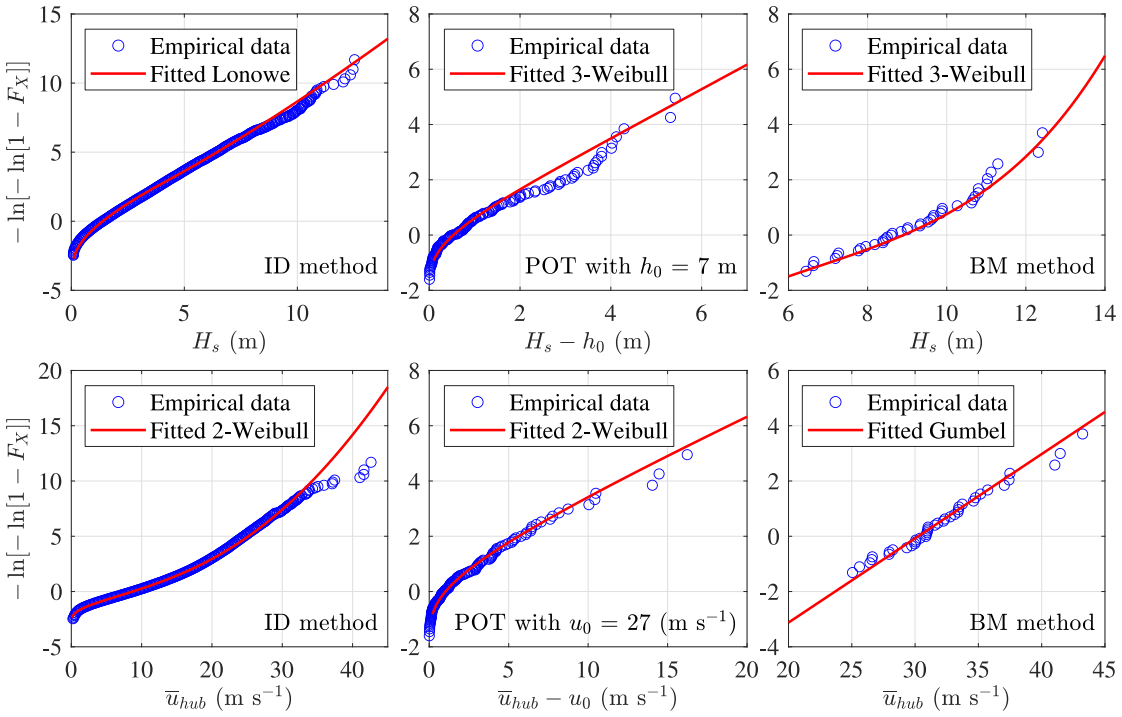

Fig. 12. Fitting of marginal H_s and $\overline{u}_{hub}$ using three methods for evaluating extremes at SN2. The fittings are plotted in the Gumbel probability paper. u_0 and h_0 are threshold values for the wind speed and significant wave height, respectively.

Table 3
Comparison of 50-year and 100-year $\overline{u}_{hub}$ (m s^{-1}) and H_s (m) using the initial distribution (ID) method, the peak over threshold (POT) method, and the block maxima (BM) methods.

Sites	SN2			UN		
	ID	POT	BM	ID	POT	BM
50-year H_s (m)	12.9	13.1	12.7	14.3	14.7	14.4
100-year H_s (m)	13.5	13.7	13.2	15.0	15.7	14.9
50-year $\overline{u}_{hub}$ (m s^{-1})	37.8	42.9	43.0	38.4	37.5	37.5
100-year $\overline{u}_{hub}$ (m s^{-1})	38.8	45.3	45.3	39.4	38.7	38.7

Table 4
Extreme mean wind speed $\overline{u}_{hub}$ and H_s corresponding to return periods of 1 year, 10 years, 50 years, and 100 years. The values in brackets present the minimum and maximum values from all grid points. The extremes are obtained based on annual maxima using the BM method.

Areas	SN2	UN
1-year H_s (m)	8.7 [8.4, 8.9]	9.6 [9.3, 9.8]
10-year H_s (m)	11.3 [10.8, 11.7]	12.8 [12.7, 13.0]
50-year H_s (m)	12.7 [12.1, 13.2]	14.4 [14.3, 14.5]
100-year H_s (m)	13.2 [12.6, 13.8]	14.9 [14.9, 15.1]
1-year $\overline{u}_{hub}$ (m s^{-1})	30.5 [30.3, 30.9]	31.0 [30.4, 31.2]
10-year $\overline{u}_{hub}$ (m s^{-1})	37.6 [37.5, 39.6]	34.7 [34.4, 35.3]
50-year $\overline{u}_{hub}$ (m s^{-1})	43.0 [42.6, 46.2]	37.5 [37.0, 38.5]
100-year $\overline{u}_{hub}$ (m s^{-1})	45.3 [44.8, 48.9]	38.7 [38.0, 39.8]

also contribute to the variations in the results. The extremes calculated using POT and BM methods in general agree well. The individual distribution methods underestimate the extreme wind speeds significantly compared to the other methods for SN2, but it results in relatively larger extreme wind speeds for UN.

To illustrate the goodness of fitting using the three methods, Fig. 12 compares the fitting of $\overline{u}_{hub}$ and H_s for SN2. Uncertainties in fitting the empirical data using all methods exist, especially in the tail regions. The few data points with extremely high values ($H_s > 12$m and $\overline{u}_{hub} > 40$ m s^{-1}) deviate from the main bulk of the data, making the fitting in the tail region challenging.

Generally, capturing the tail region with the ID method is challenging, especially for $\overline{u}_{hub}$ at SN2, leading to an underestimation of extremes relative to other methods. It is also tricky to identify which method is best due to multiple inherent uncertainties. However, the presented results cross-validate the three methods and conservative extreme values are recommended when performing ultimate load analysis.

Table 4 presents the mean, minimum and maximum values of the extremes from all grid points in the two reference sites using BM method based on annual maxima. The wave conditions are more severe at UN compared to those at SN2. However, the extreme wind speeds are higher at SN2 than at UN. The extreme values at SN2 show a higher spatial variation. For the 50-year return period, the largest difference between the extreme $\overline{u}_{hub}$ among all grid points at SN2 is 3.6 m s^{-1}, corresponding to 8% of the spatially averaged extreme value. The ratio increases slightly to 9% for the 100-year return period. The ratios are at the same level for extreme H_s at SN2. At UN, the spatial differences are less than 5% for all extreme values.

5.6. Joint distribution of wind and wave data

The joint distribution model of H_s, $\overline{u}_{hub}$ and T_p described in Section 4.5 are applied to fit the wind and wave data at the two reference sites. The fitted models are based on the spatially averaged mean wind speed at the hub height (150 m), $\overline{u}_{hub}$, the spatially averaged total sea H_s, and the spatially averaged total sea T_p. The temporal resolution of these parameters utilised in the joint distributions is 3 h. The fitted parameters and coefficients for the associated distributions are summarised in Table 5, where the corresponding equations are given. The fitted models can be used to predict extreme conditions and to generate contour lines and contour surfaces for ultimate load analysis. The models can also be applied in fatigue analysis or power production estimation of an OWF.

Fig. 13 presents 50-year contour lines of H_s and T_p for different $\overline{u}_{hub}$ levels. The contour lines are obtained through the Rosenblatt

Table 5
Parameters for the joint distribution of H_s, $\overline{u}_{hub}$ and T_p, $f_{H_s,\overline{u}_{hub},T_p}(h,u,t)$.

Distributions	Parameter	Equation	SN2	UN
Marginal H_s, $f_{H_s}(h)$	h_0	Eq. (14)	4.0	4.6
	μ_{HM}	Eq. (14)	0.520	0.569
	σ_{HM}	Eq. (14)	0.568	0.574
	α_{HM}	Eq. (14)	1.252	1.207
	β_{HM}	Eq. (14)	1.783	1.882
Conditional $\overline{u}_{hub}$ given H_s, $f_{\overline{u}_{hub}\|H_s}(u\|h)$	a_1	Eq. (16) or (17)	1.984	1.613
	a_2	Eq. (16) or (17)	0.264	0.468
	a_3	Eq. (16) or (17)	0.042	1.257
	b_1	Eq. (18)	3.972	0.461
	b_2	Eq. (18)	4.976	7.778
	b_3	Eq. (18)	0.770	0.573
Conditional T_p given H_s, $f_{T_p\|H_s}(t\|h)$	c_1	Eq. (20)	0.826	1.768
	c_2	Eq. (20)	1.0	0.276
	c_3	Eq. (20)	0.258	0.489
	d_1	Eq. (21)	0.002	0.002
	d_2	Eq. (21)	0.135	0.119
	d_3	Eq. (21)	−0.512	−0.354

Table 6
Parameters for the joint distribution of $\overline{u}_{hub}$ and Δ_θ, $f_{\overline{u}_{hub},\Delta_\theta}(u,\theta)$.

Distributions	Parameter	Equation	SN2	UN
Marginal $\overline{u}_{hub}$, $f_{\overline{u}_{hub}}(u)$	α_{UM}	Eq. (25)	2.252	2.260
	β_{UM}	Eq. (25)	12.320	13.308
	γ_{UM}	Eq. (25)	0	−1.405
Conditional Δ_θ given $\overline{u}_{hub}$, $f_{\Delta_\theta\|\overline{u}_{hub}}(\theta\|u)$	e_1	Eq. (27)	−0.017	−0.350
	e_2	Eq. (27)	−0.123	0.291
	e_3	Eq. (27)	−0.185	−0.053
	f_1	Eq. (28)	0.144	0.193
	f_2	Eq. (28)	2.345	2.112
	f_3	Eq. (28)	−0.140	−0.114

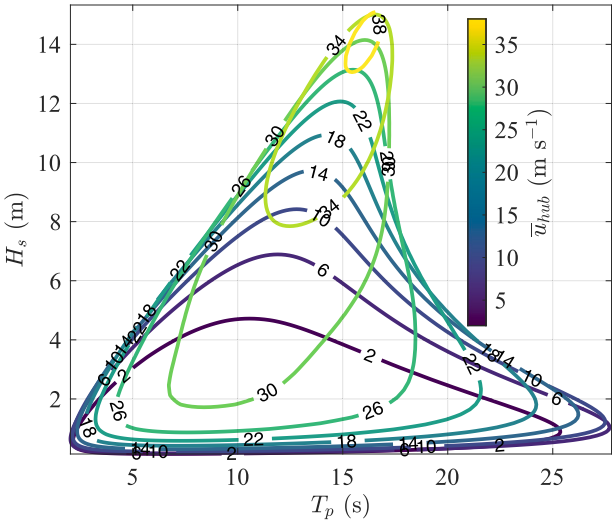

Fig. 13. Environmental contour lines of H_s and T_p for varying $\overline{u}_{hub}$ with a return period of 50 years based on the fitted parameters in Table 5; UN site.

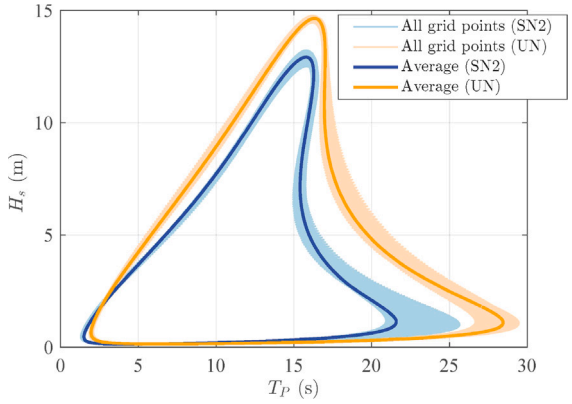

Fig. 14. Contour lines of H_s and T_p corresponding to 50-year return period of SN2 and UN. The thin lines are based on wave data from all grid points, and the thick lines are based on the spatially averaged data for which the fitted parameters are given in Table 5.

transformation of the joint distribution into a nonphysical space consisting of three independent standard Normal variables [103]. Extreme environmental conditions parameters can be selected along the contour line and then be used in efficient ultimate load prediction of offshore structures [45]. Studies of environmental contour methods for OWTs can be found in [46,104].

For structures that are only sensitive to wave conditions, two-dimensional contour lines of H_s and T_p can be used in response analysis. Fig. 14 presents the 50-year contour lines for the two reference sites based on the established joint distribution of H_s and T_p with fitted parameters in Table 5. Both the contour lines based on the wave data from all grid points and based on the spatially averaged data are shown. The spatial variations of the left parts of the contours are negligible, while there are visible variations on the right and lower parts of the contours lines, especially for SN2. These variations are partly due to the uncertainties in fitting the conditional distribution of T_p given H_s.

The fitted parameters and coefficients for the joint distribution of $\overline{u}_{hub}$ and the misalignment angle Δ_θ are summarised in Table 6. Fig. 15 presents the joint PDF of $\overline{u}_{hub}$ and Δ_θ at UN. From the joint distribution, the misalignment angle for different wind speed conditions can be extracted. To provide more information on the misalignment angle for critical wind speeds, the PDF of Δ_θ for two given wind conditions is presented. The first wind condition corresponds to the rated wind speed for the NREL 15-MW OWT with $\overline{u}_{hub}$ = 10.6 m s^{-1}, and the second

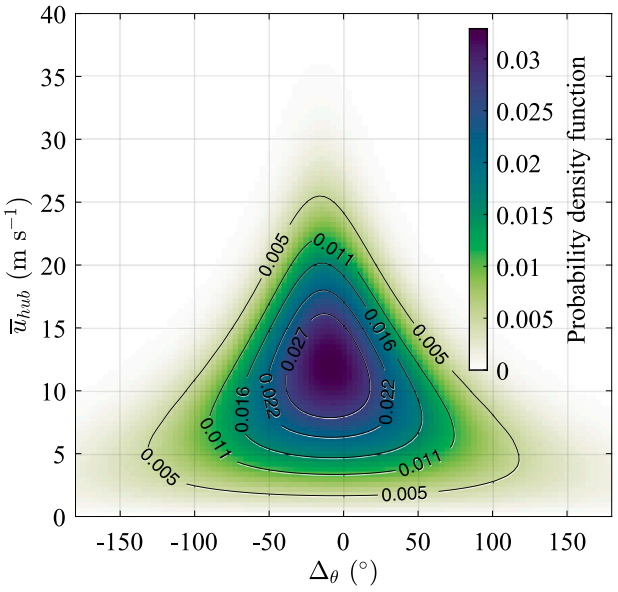

Fig. 15. Joint probability density function of $\overline{u}_{hub}$ and Δ_θ at UN based on the fitted parameters in Table 6. Note that the unit of Δ_θ in the distribution function is in radians. Here we convert the radians into degrees for the X-axis for clarity.

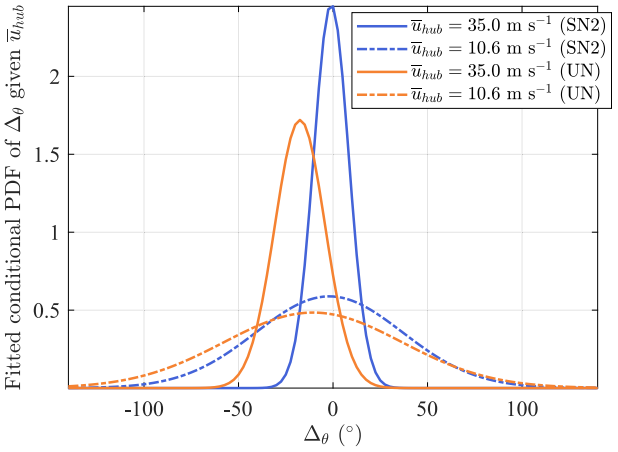

Fig. 16. Probability density function of Δ_θ at two given $\overline{u}_{hub}$ for SN2 and UN. Note that the unit of Δ_θ in the distribution function is in radians. Here we convert the radians into degrees for the X-axis for clarity.

condition corresponds to a selected extreme wind speed with $\overline{u}_{hub}$ = 35.0 m s^{-1}. The fitted conditional PDFs are shown in Fig. 16.

For both sites, the shape of the PDFs for Δ_θ at the two given wind speeds is similar, showing more spread in the misalignment angle between waves and wind under lower wind conditions. While the average misalignment angle under both wind conditions is small at SN2 (−4° for $\overline{u}_{hub}$ = 10.6 m s^{-1} and nearly zero for $\overline{u}_{hub}$ = 35.0 m s^{-1}), the average misalignment angle is larger at UN with −12° and −17° at rated wind speed and the extreme condition, respectively. The larger wind-wave misalignment at UN is likely due to the proximity of the site to the coastline. The sea depth on the South-West coast of Norway is fairly high, so no shallow water effects are expected. The coastline, however, is quite mountainous, and the land–sea temperature difference may be significant, which can amplify any misalignment between the wind and wave direction. This finding suggests potential higher dynamic responses of OWTs in the side–side direction at UN. Thus, these site-dependent properties of the metocean conditions should be properly taken into account when designing the OWFs.

It is worth mentioning that different sources of uncertainties exist when establishing joint distributions. The fitting of the conditional distributions is associated with uncertainties due to the limited data in the classes with high wind or wave conditions. For example, when fitting $\overline{u}_{hub}$ for different H_s classes, there are very few data points for H_s classes higher than 9 m, which may result in large uncertainties in the fitted two-parameter Weibull model. The choice of distribution models also introduces uncertainties, for example, the use of Normal distribution when fitting the conditional distribution of Δ_θ as discussed earlier. For analysis of extreme environmental conditions, it is recommended to concentrate on the tails instead of fitting the whole dataset. Additional discussions on the uncertainties in establishing the joint distributions can be found in Li et al. [77] and Johannessen et al. [78].

6. Application of the metocean data

The presented metocean data can be applied to assessments of OWFs at various stages of a lifecycle, e.g., design, installation, and operation and maintenance. The differences in the site features and metocean conditions of the two reference sites can affect the type of foundation and anchoring systems, layouts, maintenance strategies, and eventually the LCOE of the OWFs. In this section, we first illustrate the application through a case study using only the wave data of both reference sites from NORA3. Then, we discuss how to apply the metocean data to other research areas.

6.1. Case study of marine operations

Marine operations may be delayed due to wind speeds or wave heights exceeding the prescribed operational limits, which lead to an increased operation duration. Many critical marine operations, e.g., heavy lift operations, cannot be interrupted if the weather conditions deteriorate. In this case, the lowest allowable wind speeds or wave heights will govern the execution of the whole operation. Different marine operations have different operational limits in terms of wind speed, wave height and wave period.

In this case study, we only provide a simplified example to illustrate how to use wave data to support the planning of marine operations. The operation duration is of great concern during the planning phase of marine operations because it affects directly the operational cost. We assume a critical operation that is only dominated by waves and its operational limit is the wave height. This characteristic duration includes the operation time and the waiting time. The waiting time may account for the majority of the time if the weather conditions are poor. The total duration is measured from the day the operation is ready for launch, which is assumed to be an arbitrary day within the relevant month. A limiting value $H_s^{\max}$ = 2 m is used as an example as this threshold is specified by many installation vessels. By comparing the H_s data from NORA3 with the limiting value $H_s^{\max}$, the characteristic duration of completing critical operations with different operation duration (12 h, 24 h, and 48 h) can be estimated, as shown by Fig. 17 for the two reference sites. The duration statistics P10, P50 and P90 are also presented, where P10, P50 and P90 refer to the values corresponding to 10%, 50%, and 90% percentiles.

The characteristic duration increases greatly with operational duration, not only because of the increase in the operational time but also due to the significant increase in the waiting time, especially during winter. Comparing the results from the two reference sites, the characteristic duration is higher at UN than at SN2 due to the more severe wave conditions, indicating potentially higher operational costs at UN for performing the same tasks. The differences increase with the operational time. Moreover, the spatial variation of the duration is also more visible during the winter months at UN, due to the greater variability of H_s.

The presented case study is only one example of using metocean data in planning marine operations. In practice, a weather window

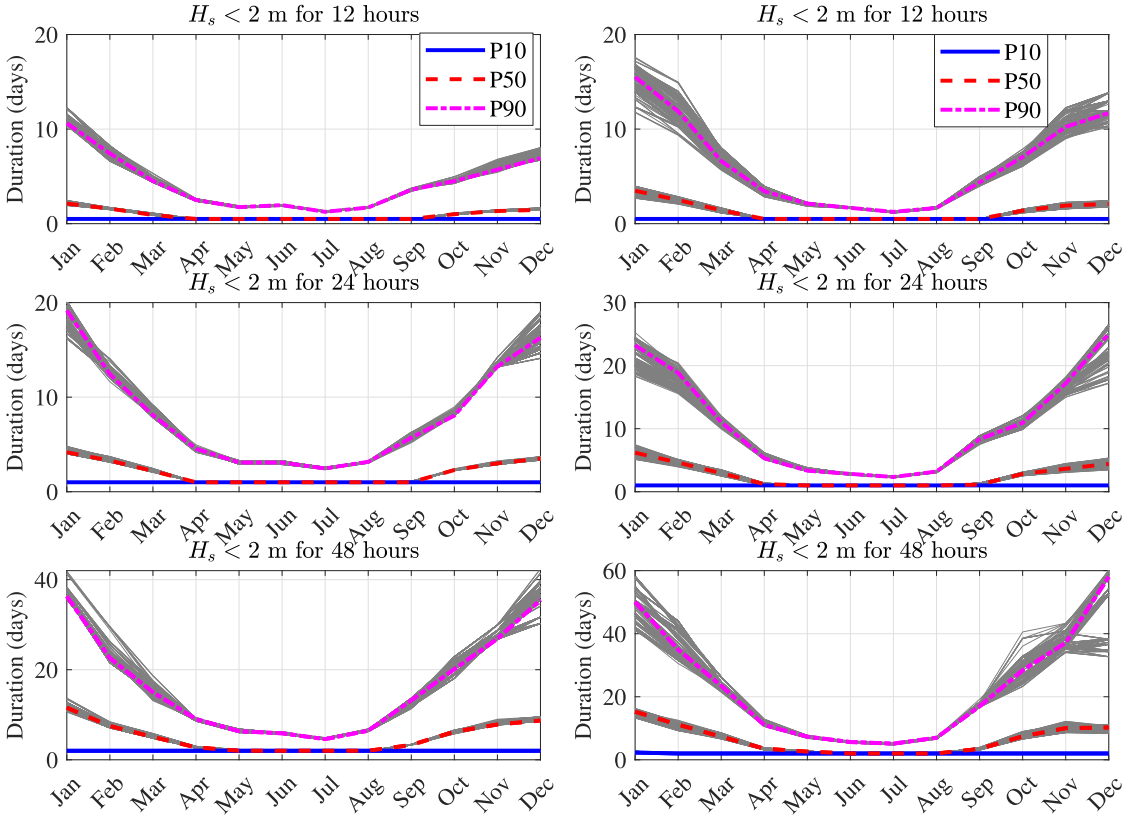

Fig. 17. Characteristic duration (including waiting time) for performing operations limited by H_s of 2 m and for different operational durations at SN2 (left panels) and UN (right panels). The grey lines are based on wave data from all grid points, and the coloured lines are based on the spatially averaged data.

analysis should be based on well-established operational limits. For marine operations using floating vessels, the wave periods and the wave spectral shape should be included in the operational limits. In addition, wind speed and directions should also be considered when the responses of the operational system are sensitive to wind speed. Due to the complexity and variability of different types of marine operations, such an assessment should be performed for all critical activities that may limit the whole operation. More examples of analyses of marine operations related to wind turbine installation activities and weather window analyses using the metocean database can be found in Guachamin-Acero et al. [34], Acero et al. [41], Li [105] or Guachamin-Acero and Li [106].

6.2. Further discussions

The metocean data discussed herein have applications beyond marine operations, notably in the structural design of wind turbine components and in layout optimisation of OWFs. We address these applications briefly below.

The IEC standard [43] recommends the use of site-specific environmental conditions for assessing the structural responses of OWTs. Given the availability of metocean data for the UN and SN2 sites, it is essential to incorporate site features in the preliminary design and analysis of wind turbine components within a farm. A comparison between the UN and SN2 sites reveals more severe wave conditions at the former, which, coupled with greater water depth, suggests the viability of implementing spar FWTs over other designs. Moreover, given the potential wind-wave misalignment exceeding 10° at UN, it may be valuable to consider structural fatigue damages in the side-to-side directions.

Both SN2 and UN can accommodate floating OWFs due to water depths close to or exceeding 60 m. However, the layout optimisation for floating OWFs poses additional challenges. In the case of tension-leg platforms, the foundations demonstrate limited horizontal movements in surge and sway, resulting in an optimisation problem akin to that for bottom-fixed wind farms. Considering spar and semi-submersible floating foundations, both wind and wave data are essential in layout optimisation. The combined effects of wind and wave actions cause floating wind turbines to shift positions within a farm, thereby influencing the wake patterns of downstream turbines. Addressing the impact of these motion patterns on analytical wake models is critical for accurate power production estimation in layout optimisation, a topic currently under-explored in literature.

7. Concluding remarks

This study presents the metocean data for two prominent areas in the Norwegian exclusive economic zone, newly available for wind energy licensing applications. The data, extracted from the NORA3 database released in 2021 encompasses two sites. The first one, Sørlige Nordsjø II, covers an area of 2591 km^2, characterised by optimal wind conditions and an average depth of 60 m. The second site, Utsira Nord, spans 1010 km^2 is situated near the Norwegian coast and is delineated by sea depths ranging from 200 to 280 m. The prospective deployment of floating offshore wind turbines at Utsira Nord may signify a major advancement for large-scale floating wind farms.

This study uses the NORA3 dataset with a 3 km horizontal and 1 h temporal resolution from 1982 to 2022, detailing wind conditions at multiple altitudes ranging from 10 m to 750 m. Data were also interpolated at a height of 150 m, which corresponds to the hub height

of turbines with capacities exceeding 13 MW. From the metocean analysis, the main conclusions include:

- Both sites, covering areas exceeding 1×10^3 km^2, demonstrate minimal spatial variability in wind conditions, thus facilitating the utilisation of spatially averaged data for metocean studies.
- The power law wind speed profile is found to have limited capability to capture the height-variability of the mean wind speed when $\overline{u}_{hub} < 12$ m s^{-1}. This finding implies that the fatigue life analysis of offshore wind turbines cannot solely rely on the power law profile. However, for stronger winds, specifically when $\overline{u}_{hub} > 15$ m s^{-1}, a Gaussian mixture model effectively depicts the power coefficient's distribution.
- Utsira Nord encounters more (less) extreme wave heights (wind speeds) compared to Sørlige Nordsjø II. A notable difference is also evident in the misalignment between wind and wave directions at Utsira Nord. These disparities, coupled with the variation in water depths, necessitate careful consideration in selecting potential foundations for offshore wind turbines.
- Joint distributions of key wind and wave parameters have been established for both sites using spatially averaged data, and the respective fitted coefficients have been documented. These distributions are crucial in creating environmental contour lines, which are used for the ultimate and fatigue limit state analysis of offshore wind turbines.
- The NORA3 database provides estimates of local vertical mean wind shear. Eq. (9) enables calculation of the standard deviation of the along-wind velocity component at a specific height. By combining the mean wind shear and velocity standard deviation, one can calculate the Mann length scale parameter L using Kelly's method [94]. This length scale parameter L is crucial in modelling wind coherence using the Mann model. As the coherence is a fundamental turbulence characteristic for wind turbine design, it could be possible to combine the NORA3 data, Eq. (9) and Kelly's method to study the coherence in the marine atmospheric boundary layer in the absence of in-situ measurements. However, Kelly's method validation primarily involves onshore, coastal data. Therefore, obtaining true offshore measurements is essential to evaluate the applicability of this method.
- Based on a preliminary case study focused on wave-sensitive marine operation, Utsira Nord is anticipated to require longer operation durations, potentially leading to higher operation and maintenance costs compared to Sørlige Nordsjø II.

Future efforts will use this metocean dataset for detailed case studies, aiding the design, analysis, and operational management of offshore wind farms. Furthermore, opportunities to apply this dataset to airborne wind energy and other marine renewable energy systems such as wave energy converters and floating solar farms remain to be explored.

CRediT authorship contribution statement

Etienne Cheynet: Conceptualization, Data curation, Formal analysis, Methodology, Software, Validation, Writing – original draft, Writing – review & editing. **Lin Li:** Conceptualization, Data curation, Formal analysis, Investigation, Methodology, Software, Validation, Writing – original draft, Writing – review & editing. **Zhiyu Jiang:** Conceptualization, Investigation, Methodology, Writing – original draft, Writing – review & editing.

Declaration of competing interest

The authors declare that they have no known competing financial interests or personal relationships that could have appeared to influence the work reported in this paper.

Data availability

The dataset for this study is available on Zenodo, licensed under BSD-3-Clause, in netcdf-4 format. It comprises three parts:

1. Metocean conditions at Utsira Nord (1982–2022) per grid point https://doi.org/10.5281/zenodo.10048048.
2. Metocean conditions at Sørilge Nordsjø II (1982–2022) per grid point https://doi.org/10.5281/zenodo.7057407.
3. Spatially averaged metocean conditions for both sites https://doi.org/10.5281/zenodo.10048159.

Acknowledgements

This work has been partly financed by UH-nett Vest 2020 (project: 72005), ImpactWind Sørvest (NFR project number: 332034) and Large Offshore Wind Turbines (LOWT) (NFR project number: 325294).

References

[1] H.D. Matthews, S. Wynes, Current global efforts are insufficient to limit warming to 1.5°C, Science 376 (6600) (2022) 1404–1409.
[2] M. Meinshausen, J. Lewis, C. McGlade, J. Gütschow, Z. Nicholls, R. Burdon, et al., Realization of Paris Agreement pledges may limit warming just below 2°C, Nature 604 (7905) (2022) 304–309.
[3] J. Bosch, I. Staffell, A.D. Hawkes, Temporally explicit and spatially resolved global offshore wind energy potentials, Energy 163 (2018) 766–781.
[4] GWEC, GWEC global wind report 2023, 2023, https://gwec.net/wp-content/uploads/2023/04/GWEC-2023_interactive.pdf. (Accessed 04 September 2023).
[5] IEA, Wind Power Generation in the Net Zero Scenario, 2015–2030, Tech. Rep., The International Energy Agency, Paris, 2023.
[6] IRENA, Renewable Power Generation Costs in 2022, Tech. Rep., The International Renewable Energy Agency, Abu Dhabi, 2022.
[7] K. Linnerud, A. Dugstad, B.J. Rygg, Do people prefer offshore to onshore wind energy? The role of ownership and intended use, Renew. Sustain. Energy Rev. 168 (2022) 112732.
[8] A.M. Østenby, Dybde og kompliserte bunnforhold gjør havvind i Norge dyrere enn i Europa, Tech. Rep., The Norwegian Water Resources and Energy Directorate, Oslo 2019, (in Norwegian).
[9] I.M. Solbrekke, A. Sorteberg, NORA3-WP: A high-resolution offshore wind power dataset for the Baltic, North, Norwegian, and Barents Seas, Sci. Data 9 (1) (2022) 362.
[10] K.S. Berg, M. Carlsen, T. Eirum, S.B. Jakobsen, N.H. Johnson, S.K. Mindeberg, et al., Havvind - Strategisk konsekvensutredning, Tech. Rep., The Norwegian Water Resources and Energy Directorate, Oslo 2012, (in Norwegian).
[11] United Nations, Theme Report on Energy Transition–Towards the Achievement of SDG 7 and Net-Zero Emissions, Tech. Rep., United Nations, New York, 2021.
[12] L. Meeus, M. Saguan, Innovating grid regulation to regulate grid innovation: From the Orkney Isles to Kriegers Flak via Italy, Renew. Energy 36 (6) (2011) 1761–1765.
[13] M. Kenis, L. Lanzilao, K. Bruninx, J. Meyers, E. Delarue, Trading rights to consume wind in presence of farm-farm interactions, Joule (2023).
[14] E. Finserås, I.H. Anchustegui, E. Cheynet, C.G. Gebhardt, J. Reuder, Gone with the wind? Wind farm-induced wakes and regulatory gaps, Marine Policy 159 (2024) 105897.
[15] H.E. Petrie, C.H. Eide, H. Haflidason, T. Watton, A conceptual geological model for offshore wind sites in former ice stream settings: the Utsira Nord site, North Sea, J. Geol. Soc. 179 (5) (2022) jgs2021–163.
[16] H. Petrie, C. Eide, H. Haflidason, T. Watton, Geological conditions for offshore wind turbine foundations at the Sørlige Nordsjø II site, Norwegian North Sea, in: EAGE GET 2022, No. 1, European Association of Geoscientists & Engineers, 2022, pp. 1–5.
[17] Z. Jiang, Installation of offshore wind turbines: A technical review, Renew. Sustain. Energy Rev. 139 (2021) 110576.
[18] Y. Guo, H. Wang, J. Lian, Review of integrated installation technologies for offshore wind turbines: Current progress and future development trends, Energy Convers. Manage. 255 (2022) 115319.
[19] A. Jacobsen, M. Godvik, Influence of wakes and atmospheric stability on the floater responses of the Hywind Scotland wind turbines, Wind Energy 24 (2) (2021) 149–161.
[20] Z. Ren, A.S. Verma, Y. Li, J.J. Teuwen, Z. Jiang, Offshore wind turbine operations and maintenance: A state-of-the-art review, Renew. Sustain. Energy Rev. 144 (2021) 110886.
[21] N. Sergiienko, L. da Silva, E. Bachynski-Polić, B. Cazzolato, M. Arjomandi, B. Ding, Review of scaling laws applied to floating offshore wind turbines, Renew. Sustain. Energy Rev. 162 (2022) 112477.

[22] A.N. Hahmann, T. Sīle, B. Witha, N.N. Davis, M. Dörenkämper, Y. Ezber, et al., The making of the New European Wind Atlas –part 1: Model sensitivity, Geosci. Model Dev. 13 (10) (2020) 5053–5078.

[23] H. Hersbach, B. Bell, P. Berrisford, S. Hirahara, A. Horányi, J. Muñoz-Sabater, et al., The ERA5 global reanalysis, Q. J. R. Meteorol. Soc. 146 (730) (2020) 1999–2049.

[24] H. Haakenstad, Ø. Breivik, B.R. Furevik, M. Reistad, P. Bohlinger, O.J. Aarnes, NORA3: A nonhydrostatic high-resolution hindcast of the North Sea, the Norwegian Sea, and the Barents Sea, J. Appl. Meteorol. Climatol. 60 (10) (2021) 1443–1464.

[25] P. Veers, K. Dykes, E. Lantz, S. Barth, C.L. Bottasso, O. Carlson, et al., Grand challenges in the science of wind energy, Science 366 (6464) (2019) eaau2027, http://dx.doi.org/10.1126/science.aau2027.

[26] P. Veers, C. Bottasso, L. Manuel, J. Naughton, L. Pao, J. Paquette, et al., Grand challenges in the design, manufacture, and operation of future wind turbine systems, Wind Energy Sci. Discuss. (2022) 1–102.

[27] H. Haakenstad, Ø. Breivik, NORA3. Part II: Precipitation and temperature statistics in complex terrain modeled with a nonhydrostatic model, J. Appl. Meteorol. Climatol. 61 (10) (2022) 1549–1572.

[28] Ø. Breivik, A. Carrasco, H. Haakenstad, O.J. Aarnes, A. Behrens, J.R. Bidlot, et al., The impact of a reduced high-wind Charnock parameter on wave growth with application to the North Sea, the Norwegian Sea, and the Arctic Ocean, J. Geophys. Res.: Oceans 127 (3) (2022) e2021JC018196.

[29] B.R. Furevik, H. Haakenstad, Near-surface marine wind profiles from rawinsonde and NORA10 hindcast, J. Geophys. Res.: Atmos. 117 (D23) (2012).

[30] I.M. Solbrekke, A. Sorteberg, H. Haakenstad, The 3 km Norwegian reanalysis (NORA3)–a validation of offshore wind resources in the North Sea and the Norwegian Sea, Wind Energy Sci. 6 (6) (2021) 1501–1519.

[31] E. Cheynet, I.M. Solbrekke, J.M. Diezel, J. Reuder, A one-year comparison of new wind atlases over the North Sea, in: Journal of Physics: Conference Series, Vol. 2362, IOP Publishing, 2022, p. 012009.

[32] G. Liang, Z. Jiang, K. Merz, Mooring analysis of a dual-spar floating wind farm with a shared line, J. Offshore Mech. Arct. Eng. 143 (6) (2021).

[33] A.S. Verma, Z. Jiang, N.P. Vedvik, Z. Gao, Z. Ren, Impact assessment of a wind turbine blade root during an offshore mating process, Eng. Struct. 180 (2019) 205–222.

[34] W. Guachamin-Acero, Z. Jiang, L. Li, Numerical study of a concept for major repair and replacement of offshore wind turbine blades, Wind Energy 23 (8) (2020) 1673–1692.

[35] K. Murthy, O. Rahi, A comprehensive review of wind resource assessment, Renew. Sustain. Energy Rev. 72 (2017) 1320–1342.

[36] G. Gualtieri, Analysing the uncertainties of reanalysis data used for wind resource assessment: A critical review, Renew. Sustain. Energy Rev. 167 (2022) 112741.

[37] M.M. Nezhad, M. Neshat, G. Piras, D.A. Garcia, Sites exploring prioritisation of offshore wind energy potential and mapping for wind farms installation: Iranian islands case studies, Renew. Sustain. Energy Rev. 168 (2022) 112791.

[38] BNEF, Cost of new renewables temporarily rises as inflation starts to bite, 2022, https://about.bnef.com/blog/cost-of-new-renewables-temporarily-rises-as-inflation-starts-to-bite/. (Accessed 15 August 2022).

[39] A. Martinez, G. Iglesias, Mapping of the levelised cost of energy for floating offshore wind in the European Atlantic, Renew. Sustain. Energy Rev. 154 (2022) 111889.

[40] M. Lerch, M. De-Prada-Gil, C. Molins, The influence of different wind and wave conditions on the energy yield and downtime of a spar-buoy floating wind turbine, Renew. Energy 136 (2019) 1–14.

[41] W.G. Acero, L. Li, Z. Gao, T. Moan, Methodology for assessment of the operational limits and operability of marine operations, Ocean Eng. 125 (2016) 308–327.

[42] Z. Jiang, W. Hu, W. Dong, Z. Gao, Z. Ren, Structural reliability analysis of wind turbines: A review, Energies 10 (12) (2017) 2099.

[43] IEC, Wind Turbines—Part 3: Design Requirements for Offshore Wind Turbines, 2009.

[44] DNV, Floating Wind Turbine Structures (DNV-ST-0119), Det Norske Veritas AS, Oslo, 2009.

[45] S.R. Winterstein, T.C. Ude, C.A. Cornell, P. Bjerager, S. Haver, Environmental parameters for extreme response: Inverse FORM with omission factors, in: Proceedings of the ICOSSAR-93, Innsbruck, Austria, 1993, pp. 551–557.

[46] Q. Li, Z. Gao, T. Moan, Modified environmental contour method for predicting long-term extreme responses of bottom-fixed offshore wind turbines, Mar. Struct. 48 (2016) 15–32.

[47] W. Dong, T. Moan, Z. Gao, Long-term fatigue analysis of multi-planar tubular joints for jacket-type offshore wind turbine in time domain, Eng. Struct. 33 (6) (2011) 2002–2014.

[48] Z. Jiang, Y. Xing, Load mitigation method for wind turbines during emergency shutdowns, Renew. Energy 185 (2022) 978–995.

[49] R. Shakoor, M.Y. Hassan, A. Raheem, Y.K. Wu, Wake effect modeling: A review of wind farm layout optimization using jensen' s model, Renew. Sustain. Energy Rev. 58 (2016) 1048–1059.

[50] A. Pillai, J. Chick, L. Johanning, M. Khorasanchi, V. De Laleu, Offshore wind farm electrical cable layout optimization, Eng. Optim. 47 (12) (2015) 1689–1708.

[51] P. Hou, J. Zhu, K. Ma, G. Yang, W. Hu, Z. Chen, A review of offshore wind farm layout optimization and electrical system design methods, J. Mod. Power Syst. Clean Energy 7 (5) (2019) 975–986.

[52] A.P. Stanley, A. Ning, Massive simplification of the wind farm layout optimization problem, Wind Energy Sci. 4 (4) (2019) 663–676.

[53] A. Niayifar, F. Porté-Agel, Analytical modeling of wind farms: A new approach for power prediction, Energies 9 (9) (2016) 741.

[54] J. Feng, W.Z. Shen, Modelling wind for wind farm layout optimization using joint distribution of wind speed and wind direction, Energies 8 (4) (2015) 3075–3092.

[55] P.A. Fleming, A. Ning, P.M. Gebraad, K. Dykes, Wind plant system engineering through optimization of layout and yaw control, Wind Energy 19 (2) (2016) 329–344.

[56] M.M. Pedersen, P. van der Laan, M. Friis-Møller, J. Rinker, P.E. Réthoré, DTUWindEnergy/PyWake: PyWake, Zenodo, 2019, http://dx.doi.org/10.5281/zenodo.2562662.

[57] L. Lanzilao, J. Meyers, A new wake-merging method for wind-farm power prediction in the presence of heterogeneous background velocity fields, Wind Energy 25 (2) (2022) 237–259.

[58] Y. Rubner, C. Tomasi, L.J. Guibas, The earth mover's distance as a metric for image retrieval, Int. J. Comput. Vis. 40 (2) (2000) 99–121.

[59] IEC 61400-1, Wind Turbines Part 1; Design Requirements, International Electrotechnical Committee, Geneva, Switzerland, 2005.

[60] J. Fischereit, R. Brown, X.G. Larsén, J. Badger, G. Hawkes, Review of mesoscale wind-farm parametrizations and their applications, Bound.-Lay. Meteorol. 182 (2) (2022) 175–224.

[61] D. Deaves, R. Harris, A note on the use of asymptotic similarity theory in neutral atmospheric boundary layers, Atmos. Environ. (1967) 16 (8) (1982) 1889–1893.

[62] ESDU, in: IHS ESDU (Ed.), ESDU 85020, Characteristics of Atmospheric Turbulence near the Ground. Part II: Single Point Data for Strong Winds (Neutral Atmosphere), 2001.

[63] J.S. Touma, Dependence of the wind profile power law on stability for various locations, J. Air Pollut. Control Assoc. 27 (9) (1977) 863–866.

[64] S.N. Gadde, R.J. Stevens, Effect of low-level jet height on wind farm performance, J. Renew. Sustain. Energy 13 (1) (2021) 013305.

[65] H. Charnock, Wind stress on a water surface, Q. J. R. Meteorol. Soc. 81 (350) (1955) 639–640.

[66] E.B. Kraus, J.A. Businger, Atmosphere-Ocean Interaction, vol. 27, Oxford University Press, 1994.

[67] D.Y. Kim, Y.H. Kim, B.S. Kim, Changes in wind turbine power characteristics and annual energy production due to atmospheric stability, turbulence intensity, and wind shear, Energy 214 (2021) 119051.

[68] I.A. Renfrew, C. Barrell, A. Elvidge, J. Brooke, C. Duscha, J. King, et al., An evaluation of surface meteorology and fluxes over the Iceland and Greenland Seas in ERA5 reanalysis: The impact of sea ice distribution, Q. J. R. Meteorol. Soc. 147 (734) (2021) 691–712.

[69] J.C. Kaimal, J.J. Finnigan, Atmospheric Boundary Layer Flows: Their Structure and Measurement, Oxford University Press, 1994.

[70] M. Türk, S. Emeis, The dependence of offshore turbulence intensity on wind speed, J. Wind Eng. Ind. Aerodyn. 98 (8–9) (2010) 466–471.

[71] NORSOK, NORSOK Standard N-003: Actions and action effects, Stand. Nor. (2007).

[72] O.J. Andersen, J. Løvseth, The Frøya database and maritime boundary layer wind description, Mar. Struct. 19 (2–3) (2006) 173–192.

[73] DNV, Environmental Conditions and Environmental Loads (DNV-RP-C205), Det Norske Veritas AS, Oslo, 2014.

[74] S. Haver, Analysis of Uncertainties Related to the Stochastic Modelling of Ocean Waves (Ph.D. thesis), Norwegian Institute of Technology, Trondheim, Norway, 1980.

[75] E. Bitner-Gregersen, S. Haver, Joint long term description of environmental parameters for structural response calculation, in: Proceedings of the 2nd International Workshop on Wave Hindcasting and Forecasting, 1989, pp. 25–28.

[76] E.M. Bitner-Gregersen, S. Haver, Joint environmental model for reliability calculations, in: The First International Offshore and Polar Engineering Conference, OnePetro, 1991, pp. 246–253.

[77] L. Li, Z. Gao, T. Moan, Joint distribution of environmental condition at five European offshore sites for design of combined wind and wave energy devices, J. Offshore Mech. Arct. Eng. 137 (3) (2015).

[78] K. Johannessen, T.S. Meling, S. Hayer, Joint distribution for wind and waves in the northern North Sea, in: The Eleventh International Offshore and Polar Engineering Conference, OnePetro, 2001, pp. 19–28.

[79] L. Barj, J.M. Jonkman, A. Robertson, G.M. Stewart, M.A. Lackner, L. Haid, et al., Wind/wave misalignment in the loads analysis of a floating offshore wind turbine, in: 32nd ASME Wind Energy Symposium, 2014, p. 0363.

[80] E.E. Bachynski, M.I. Kvittem, C. Luan, T. Moan, Wind-wave misalignment effects on floating wind turbines: motions and tower load effects, J. Offshore Mech. Arct. Eng. 136 (4) (2014).

[81] E.M. Bitner-Gregersen, Distribution of Multidirectional Environmental Effects, Tech. Rep., American Society of Mechanical Engineers, United States, 1996.
[82] G.M. Stewart, M.A. Lackner, The impact of passive tuned mass dampers and wind–wave misalignment on offshore wind turbine loads, Eng. Struct. 73 (2014) 54–61.
[83] J.T.H. Horn, J.R. Krokstad, J. Amdahl, Joint probability distribution of environmental conditions for design of offshore wind turbines, in: International Conference on Offshore Mechanics and Arctic Engineering, Vol. 57786, American Society of Mechanical Engineers, 2017, p. V010T09A068.
[84] S. Porchetta, D. Muñoz-Esparza, W. Munters, J. van Beeck, N. van Lipzig, Impact of ocean waves on offshore wind farm power production, Renew. Energy 180 (2021) 1179–1193.
[85] D. Ahsan, S. Pedersen, The influence of stakeholder groups in operation and maintenance services of offshore wind farms: Lesson from Denmark, Renew. Energy 125 (2018) 819–828.
[86] M. Wu, Numerical analysis of docking operation between service vessels and offshore wind turbines, Ocean Eng. 91 (2014) 379–388.
[87] R.J. Rossi, Mathematical Statistics: An Introduction to Likelihood Based Inference, John Wiley & Sons, 2018.
[88] B.R. Furevik, H. Haakenstad, Near-surface marine wind profiles from rawinsonde and NORA10 hindcast, J. Geophys. Res.: Atmos. 117 (D23) (2012).
[89] S. Hsu, E.A. Meindl, D.B. Gilhousen, Determining the power-law wind-profile exponent under near-neutral stability conditions at sea, J. Appl. Meteorol. Climatol. 33 (6) (1994) 757–765.
[90] G. Gualtieri, A comprehensive review on wind resource extrapolation models applied in wind energy, Renew. Sustain. Energy Rev. 102 (2019) 215–233.
[91] J.J. Tieo, M. Skote, N. Srikanth, Suitability of power-law extrapolation for wind speed estimation on a tropical island, J. Wind Eng. Ind. Aerodyn. 205 (2020) 104317.
[92] E. Cheynet, J.B. Jakobsen, J. Reuder, Velocity spectra and coherence estimates in the marine atmospheric boundary layer, Bound-Layer Meteorol. 169 (3) (2018) 429–460.
[93] J. Mann, The spatial structure of neutral atmospheric surface-layer turbulence, J. Fluid Mech. 273 (1994) 141–168.
[94] M. Kelly, From standard wind measurements to spectral characterization: turbulence length scale and distribution, Wind Energy Sci. 3 (2) (2018) 533–543.
[95] A. Sathe, J. Mann, T. Barlas, W. Bierbooms, G. Van Bussel, Influence of atmospheric stability on wind turbine loads, Wind Energy 16 (7) (2013) 1013–1032.
[96] M. Holtslag, W. Bierbooms, G. Van Bussel, Wind turbine fatigue loads as a function of atmospheric conditions offshore, Wind Energy 19 (10) (2016) 1917–1932.
[97] R.M. Putri, C. Obhrai, J.B. Jakobsen, M.C. Ong, Numerical analysis of the effect of offshore turbulent wind inflow on the response of a spar wind turbine, Energies 13 (10) (2020) 2506.
[98] A. Nybø, F. Gunnar Nielsen, M. Godvik, Sensitivity of the dynamic response of a multimegawatt floating wind turbine to the choice of turbulence model, Wind Energy (2022).
[99] I. Rivera-Arreba, A.S. Wise, M. Hermile, F.K. Chow, E.E. Bachynski-Polić, Effects of atmospheric stability on the structural response of a 12 MW semisubmersible floating wind turbine, Wind Energy (2022).
[100] E. Cheynet, M. Flügge, J. Reuder, J.B. Jakobsen, Y. Heggelund, B. Svardal, et al., The COTUR project: remote sensing of offshore turbulence for wind energy application, Atmos. Meas. Tech. 14 (9) (2021) 6137–6157.
[101] E.B. Mackay, P.G. Challenor, A.S. Bahaj, A comparison of estimators for the generalised Pareto distribution, Ocean Eng. 38 (11–12) (2011) 1338–1346.
[102] E. Vanem, Uncertainties in extreme value modelling of wave data in a climate change perspective, J. Ocean Eng. Mar. Energy 1 (2015) 339–359.
[103] H.O. Madsen, S. Krenk, N.C. Lind, Methods of Structural Safety, Courier Corporation, 2006.
[104] X. Chen, Z. Jiang, Q. Li, Y. Li, N. Ren, Extended environmental contour methods for long-term extreme response analysis of offshore wind turbines, J. Offshore Mech. Arct. Eng. 142 (5) (2020) 052003.
[105] L. Li, Dynamic Analysis of the Installation of Monopiles for Offshore Wind Turbines (Ph.D. thesis), Norwegian University of Science and Technology, Norway, 2016.
[106] W. Guachamin-Acero, L. Li, Methodology for assessment of operational limits including uncertainties in wave spectral energy distribution for safe execution of marine operations, Ocean Eng. 165 (2018) 184–193.